

Title: The proteasome controls ESCRT-III mediated cell division in an archaeon

Authors: Gabriel Tarrason Risa^{1†}, Fredrik Hurtig^{2†}, Sian Bray³, Anne E. Hafner^{1,4,5}, Lena Harker-Kirschneck^{1,4,5}, Peter Faull⁶, Colin Davis⁶, Dimitra Papatziadou⁷, Delyan R. Mutavchiev¹, Catherine Fan¹, Leticia Meneguello¹, Andre Arashiro Pulschen¹, Gautam Dey¹, Siân Culley¹, Mairi Kilkenny³, Diorge P. Souza¹, Luca Pellegrini³, Robertus A. M. de Bruin¹, Ricardo Henriques¹, Ambrosius P. Snijders⁶, Anđela Šarić^{1,4,5}, Ann-Christin Lindås², Nicholas P. Robinson^{7*} and Buzz Baum^{1,4*}

Affiliations:

¹ MRC-Laboratory for Molecular Cell Biology, UCL, Gower Street, London, UK.

² Department of Molecular Biosciences, The Wenner-Gren Institute, Stockholm University, Sweden

³ Biochemistry Department, University of Cambridge, UK

⁴ Institute for the Physics of Living Systems, UCL, UK

⁵ Department of Physics and Astronomy, UCL, UK

⁶ Proteomics platform, The Francis Crick Institute, Midlands Road, London, UK

⁷ Faculty of Health and Medicine, Division of Biomedical and Life Sciences, Lancaster University, UK

†These authors contributed equally

*Correspondence to: b.baum@ucl.ac.uk; n.robinson2@lancaster.ac.uk

Abstract: *Sulfolobus acidocaldarius* is the closest experimentally tractable archaeal relative of eukaryotes and, despite lacking obvious CDK/Cyclin homologues, has an ordered eukaryote-like cell cycle with distinct phases of DNA replication and division. Here, in exploring the mechanism of cell division in *S. acidocaldarius*, we identify a role for the archaeal proteasome in regulating the transition from the end of one cell cycle to the beginning of the next. Further, we identify the archaeal ESCRT-III homologue, CdvB, as a key target of the proteasome, and show that its degradation triggers division by allowing constriction of the CdvB1:CdvB2 ESCRT-III division ring. These findings offer a minimal mechanism for ESCRT-III mediated membrane remodelling and point to a conserved role for the proteasome in eukaryotic and archaeal cell cycle control.

One Sentence Summary: This study identifies a role for the proteasome in controlling the cell cycle and triggering ESCRT-III mediated cell division in an archaeon.

Introduction: The eukaryotic cell cycle is ordered by oscillations in the activity of a conserved set of Cyclin-dependent kinases. While both Cyclins and Cyclin-dependent kinases have yet to be identified outside of eukaryotes, *S. acidocaldarius* within the TACK (Thaumarchaeota, Aigarchaeota, Crenarchaeota, and Korarchaeota) superphylum of archaea possess an ordered cell cycle with distinct phases of DNA replication and division, similar in structure to the cell cycle observed in many eukaryotes (1). Several of the enzymes used to drive key events in the cell cycle are also conserved from archaea to eukaryotes. For example, archaeal homologues of eukaryotic Cdc6/Orc/MCM/GINS proteins initiate DNA replication at multiple origins in *S. acidocaldarius*, just as they do in eukaryotes (2, 3). Additionally, previous work shows that homologues of ESCRT-III and the AAA+ ATPase Vps4, proteins that mediate abscission and other membrane remodelling processes in eukaryotes, play an important role in TACK archaeal cell division (4). These observations beg the question: are any of these common events regulated by conserved elements of the cell cycle control machinery that are shared across archaea and eukaryotes?

While archaea lack clear homologues of both Cyclins and Cyclin-dependent kinases, archaeal homologues of the 20S core eukaryotic proteasome are readily identifiable (5–7). This similarity in core proteasome structure sets these two branches of biology apart from bacteria (8). In eukaryotes, cell division is initiated by activation of the ubiquitin-E3 ligase, APC, which triggers proteasome-mediated degradation of Cyclin B and Securin and likely a host of other proteins

(9), leading to irreversible mitotic exit (10), chromosome segregation, and cytokinesis (11, 12). This led us to test whether proteasome-mediated degradation also plays a role in regulating the cell cycle reset in TACK archaea (1).

Here, we report that proteasomal activity is required for *S. acidocaldarius* cell division, using inhibitors of the 20S proteasome. Proteomics analyses identified a single archaeal ESCRT-III homologue, CdvB (Saci_1373), as a key target for proteasome-mediated degradation during the final stages of the cell division cycle. CdvB is part of the CdvABC operon (Saci_1374, Saci_1373 and Saci_1372) and has previously been implicated in *S. acidocaldarius* cell division (13–15). A combination of microscopy and flow cytometry data further suggested that CdvB both templates the assembly of a contractile ESCRT-III co-polymer, comprised of the paralogues CdvB1 (Saci_0451) and CdvB2 (Saci_1416), and prevents their constriction. As a consequence, proteasome-mediated degradation of CdvB triggers cell division.

Results

Bortezomib inhibits the *S. acidocaldarius* proteasome

To determine a detailed structure of the *S. acidocaldarius* proteasome, building on previous work (16), we co-expressed the α -subunit and N-terminally truncated β -subunit of the proteasome (Saci_0613 and Saci_0662 Δ N). This enabled us to produce diffracting crystals of

the catalytically inactive, twenty-eight subunit 20S proteasome, allowing us to determine its structure to a resolution of 3.7Å (Fig. 1A, Fig. S1A-C, Fig. S2A-C, Table S1, PDB ID: 6Z46). Structures of the equivalent complexes from the euryarchaeon *Archaeoglobus fulgidus* (PDB ID: 1J2Q) and *Saccharomyces cerevisiae* (PDB ID: 4NNN) were then used to generate a homology model of an N-terminally truncated catalytically active β -subunit (Saci_0909 Δ N), which was docked into the structure of the *S. acidocaldarius* proteasome in place of one inactive β -subunit (Saci_0662 Δ N) (see Methods) (17). It was then possible to dock bortezomib (PS-341, Velcade), an established reversible small molecule inhibitor of the proteasomes of euryarchaeota and eukaryotes (18–20), into the model's active site (Fig. 1B, Fig S1D-E). Here, the boronic acid moiety of bortezomib forms a bond with the nucleophilic hydroxyl group of the active site threonine, indicating that the small molecule is likely able to inhibit the proteolytic activity of the *S. acidocaldarius* 20S proteasome as it does in eukaryotes and in the euryarchaeon *Haloferax volcanii* (20, 21).

To determine whether bortezomib can inhibit the *S. acidocaldarius* proteasome in vitro, as suggested by this structural analysis, we examined the ability of the active complex (consisting of α -subunits, together with N-terminally truncated structural and catalytically active β -subunits (Saci_0613/Saci_0662 Δ N/Saci_0909 Δ N)) to degrade a Urm1-tagged GFP substrate, using a biochemical setup we described previously (see Methods) (16). When this assay was carried out with different concentrations of inhibitor, substrate degradation was found to be sensitive to bortezomib (Fig. 1C; Fig. S3A-D). We then mutated a conserved valine residue (V49) that

mediates critical contacts between the active site and the inhibitor (22) to a threonine (V49T). As expected, this led to a reduction in the sensitivity of the purified *S. acidocaldarius* 20S proteasome to bortezomib (Fig. S3E-F), validating the mode of inhibitor action.

Proteasomal inhibition arrests the cell cycle of *S. acidocaldarius*

Having demonstrated that bortezomib inhibits the *S. acidocaldarius* 20S proteasome activity in vitro, bortezomib was added to *S. acidocaldarius* cultures to look for a possible role for the 20S proteasome in cell cycle control. For this experiment, cells were synchronised in G2 using acetic acid, released, and observed by flow cytometry as they re-entered the cell cycle and divided (see Methods) (23). Strikingly, when bortezomib was added to cultures 80 minutes after release from the acetic acid arrest, the cells failed to divide (Fig. 1D, Fig. S4A-B). Furthermore, this bortezomib-induced cell cycle arrest was accompanied by a two-fold enrichment in the number of cells harbouring compact and separated nucleoids (relative to those treated with the DMSO solvent, Fig. 1E-F). While a similar arrest was observed in cells treated with MG132, a second proteasome inhibitor, this arrest proved more readily reversible, as expected given the reported K_i values of bortezomib and MG132 (0.6 nM and 4 nM, respectively) (Fig. S5A).

To test whether pre-division cells treated with bortezomib were inhibited from undergoing DNA replication as well as cell division, as is the case for a proteasome-inhibition induced mitotic arrest in eukaryotes, we made use of a *S. acidocaldarius* mutant strain expressing thymidine

kinase (STK). STK cells incorporate the thymidine analogue 5-Ethynyl-2'-deoxyuridine (EdU) into newly synthesised DNA, which can be visualised with click-it chemistry (See methods) (24). Using this assay, the majority of synchronised STK cells divided and incorporated EdU into their DNA as they entered S-phase (note that EdU prevents the completion of S-phase in *S. acidocaldarius* (24)). By contrast, there was no evidence of Edu incorporation, and therefore DNA synthesis, in cells treated with bortezomib prior to division (Fig. 1G-H, Fig. S4C-D). When bortezomib was added to synchronous cultures at a later stage to inhibit the proteasome in newly divided cells, however, these G1 cells continued unimpeded into S-phase and G2 (Fig. S4E). These data indicate that inhibiting proteasome activity specifically prohibits cells from dividing and also, directly or indirectly, from initiating the next round of DNA replication.

CdvB is targeted by the proteasome during cell division

Having observed cell cycle arrest upon proteasome inhibition (with bortezomib and MG132), we set out to identify proteins that are subject to proteasome-mediated degradation during cell division using tandem mass tag (TMT) labelling and quantitative mass spectrometry. Hits were identified by comparing the proteomes of bortezomib-treated synchronised cultures enriched for cells arrested prior to division with cultures 15 minutes after inhibitor wash-out, at which point most arrested cells had divided (see Methods). Strikingly, among the large set of proteins sampled by mass spectrometry, the protein that underwent the greatest drop in level upon release from the arrest was CdvB, an ESCRT-III homologue previously identified as a

component of the archaeal division machinery (13–15, 25) (Fig. 2A, Table S6). As expected, CdvB was also identified among the top hits when the proteome of MG132-treated pre-division cultures were compared to the proteome of DMSO-treated controls (Fig. S5B, Table S7). These results were confirmed by Western blotting using antibodies validated against cell extracts and purified proteins (Figure 2B, Fig. S6A-B, Fig. S7B; see Methods). Furthermore, CdvB levels increased markedly in cells following induced expression of a Walker B dominant-negative PAN AAA+ ATPase (Saci_0656), a protein known to cap the 20S proteasome which aids protein degradation by threading proteins into its core (8) (Fig. 2C). Notably, CdvB was the only division protein significantly enriched in these experiments (Fig. 2A, Fig. S5A, Fig. S7B). CdvA (Saci_1374, an archaea specific ESCRT-III recruitment protein), CdvC (Saci_1372, a Vps4 homologue), and CdvB1 and CdvB2 (Saci_0451, Saci_1416, ESCRT-III homologues), were largely unaffected by proteasome inhibition. This selectivity was not due to differences in Cdv gene transcription, since all of these components of the cell division machinery are transcribed as part of the same pre-division wave (13, 14) which, we confirmed, remains active during a bortezomib-induced pre-division arrest (Fig. S7A). Taken together, these observations imply a role for the selective proteasome-mediated degradation of CdvB at division.

We observed a similar sudden loss of CdvB protein from cells when we used flow cytometry to assess the levels of different ESCRT-III proteins in a population of unperturbed cells as they underwent division (see Methods). Again, CdvB was found accumulating to high levels in pre-

division cells, but was absent from newly divided G1 cells (Fig. 2D, and Fig. S8C). By contrast, CdvB1 and CdvB2 levels were maintained at high levels throughout the division process, and then partitioned between newly divided daughter cells (Fig. 2E, Fig. S8A, Fig. S8D, Fig. S8F). In examining the dynamics of CdvB and CdvB1 levels during cell division, it also became clear that CdvB was degraded in cells with 2N DNA content, i.e. prior to cell division (Fig. 2F-G, Fig. S8E, Fig. S10C). As expected, a flow cytometry analysis of CdvB levels revealed elevated levels in cells arrested prior to division by bortezomib (Fig. 2H), whereas median levels of CdvB1 and CdvB2 remained unaltered (Fig. 2I-K, Fig. S8B). Taken together, these observations show that CdvB is selectively targeted for proteasome-mediated degradation part way through the division process.

CdvB degradation triggers constriction of the CdvB1:CdvB2 ring

Previous studies have suggested that CdvB, an essential gene in *S. acidocaldarius*, is actively required for division (13–15, 25, 26). By contrast, our data suggested that the protein is degraded during division. To reconcile these data and understand the role of CdvB and its degradation in cell division, we employed SRRF super-resolution microscopy to image the archaeal ESCRT-III division rings at different stages in the division process (see Methods) (27, 28). This revealed three distinct categories of ESCRT-III division rings: 1) CdvB rings that lack CdvB1, 2) rings with co-localised CdvB and CdvB1, and 3) CdvB1 rings that lack CdvB (Fig. 3A). Conspicuously, cells harbouring a CdvB1 ring, but lacking CdvB signal, were the only ones

seen in a state of constriction. These data support a role for the selective proteasome-mediated degradation of CdvB from pre-assembled CdvB:CdvB1 rings. This is consistent with the fact that CdvB rings had a mean diameter of 1.23 μm ($n = 496$, $\text{SD} = 0.15$) (Fig. 3B), CdvB1 rings co-staining for CdvB had a near identical mean diameter of 1.24 μm ($n = 285$, $\text{SD} = 0.17$), whereas CdvB1 rings that lacked CdvB tended to be variable in size and smaller (mean = 0.62 μm , $n = 61$, $\text{SD} = 0.35$) (Fig. 3C). Moreover, as expected for a division ring, the diameter of the CdvB1 ring was nearly perfectly correlated with the diameter of the division neck, as measured by concanavalin A staining of the archaeal S-layer (Fig. S8H). Finally, the diameters of CdvB1 and CdvB2 rings were near perfectly correlated in all images, suggesting that the two ESCRT-III homologues work together during the ring constriction stage of the division process ($N = 399$, $r = 0.98$, $p = 2.2e^{-16}$) (Fig. S8H). Taken together, these data suggest that constriction is triggered by the selective and rapid degradation of CdvB by the proteasome. In line with this thinking, we were unable to detect CdvB1 rings lacking CdvB (or CdvB2 rings lacking CdvB) in cells following treatment with the proteasome inhibitor bortezomib. Moreover, all of the rings in bortezomib treated cells had a mean diameter equivalent to the uniform width of CdvB rings that span the longest axis of the cell, highlighting the role of the proteasome-mediated degradation of CdvB in triggering cell constriction (mean = 1.23 μm , $N = 346$, $\text{SD} = 0.32$) (Fig. 3D).

The flow cytometry profiles of exponentially growing asynchronous populations co-stained for CdvB and CdvB1 could also be used to generate an approximate timeline of cell division events. This revealed populations of cells in three distinct phases of the division process: 1) 2N cells with peak levels of CdvB, but low CdvB1, 2) 2N cells with peak levels of both CdvB and CdvB1,

and 3) 2N cells with falling levels of CdvB that retain peak levels of CdvB1 (Fig. S9A). Since the doubling time of these *S. acidocaldarius* cultures was about 2 hours and 45 minutes, the relative sizes of these sub-populations could be used to calculate the time spent by a typical cell as it passes through each stage in the division process. Notably, this requires taking the exponential age distribution resulting from binary division into account (Fig. S9B) (29). In this way, the entire process of ESCRT-III mediated cell division was estimated to have a duration of ~6.2 minutes (Figure 9B-C) (29). The division process was further resolved on the basis of these data to reveal the following sequence of events: i) CdvB rings had an average lifetime of ~2.6 minutes, prior to the assembly of CdvB1, ii) CdvB:CdvB1 rings then persisted for ~1.8 minutes, before CdvB was degraded by the proteasome, ii) causing CdvB1 rings to constrict within a period of ~1.8 minutes. While we observed minor variations in the percentage of cells in the other two stages of division, the percentage of cells in the contractile phase of the division process (as CdvB is being degraded) appeared highly reproducible (Fig. S9C).

Physical model of ESCRT-III mediated cell division in archaea

To better monitor changes in both the levels and localisation of the CdvB1 ring during the final stages of the division process, we imaged fixed cells via linear structured illumination microscopy (see iSIM Methods). This revealed that constriction of the CdvB1 division ring was accompanied both by an increase in the intensity of the fluorescent signal at the neck and a concomitant increase in the level of the diffuse cytoplasmic signal (Fig. 4A, Fig. S10A).

Throughout division, the sum intensity of CdvB1 remained constant (Fig. S10B). As a result, newly divided cells had high levels of diffuse CdvB1 (something we never observed imaging CdvB), in line with the flow cytometric data (Fig 2F, Fig. S8C-D). The absence of large polymeric CdvB1:CdvB2 structures in these early G1 cells, implies that CdvB1 and CdvB2 do not form *de novo* ESCRT-III filaments without a CdvB template. In keeping with this conclusion, CdvB2 appeared diffuse when it was ectopically expressed in cells arrested in G2 with acetic acid, a treatment that inhibits the expression of endogenous Cdv proteins (Fig. S11A-C). Taken together, these observations suggest that the division machinery follows a fixed sequence in which CdvB initially forms an ESCRT-III ring (in a process that likely depends on CdvA (25, 30)), which then templates the assembly of CdvB1:CdvB2 rings. This CdvB1:CdvB2 ring constricts following the sudden removal and degradation of CdvB, and is then disassembled during the division process.

To test whether these findings provide a plausible physical mechanism for *S. acidocaldarius* cell division, we used these data as the basis for a coarse-grained molecular dynamics model of ESCRT-III mediated cell division, based on a recently developed physical model of ESCRT-III dependent membrane scission (31) (see Methods). In these simulations, a modelled filament, representing the division ring, was allowed to associate with the plasma membrane of a cell modelled in 3D through its membrane-binding interface. To model the division process, we defined two different preferred filament conformations: a CdvB1 (CdvB+) state with low

curvature (defined by a large preferred radius R_0), and a CdvB1 (CdvB-) state with high curvature (defined by the small target radius R_{target}) (Fig. 4B). In this model, the transition between the initial CdvB1 (CdvB+) state and the CdvB1 (CdvB-) state represents the rapid loss of CdvB, which was modelled by an instantaneous shortening of the bonds connecting neighbouring elements in the filament. While the constriction of the CdvB1 ESCRT-III filament was able to rapidly reduce the cell circumference in these simulations, it was not sufficient to induce division because of the steric hindrance of filaments at the neck (Fig. 4C) (Movie S1, where $R_{\text{target}}/R_0 = 5\%$). This is a generic problem faced by molecular machines cutting membrane tubes from the inside. Thus, it was only when CdvB1 filaments were allowed to disassemble as they constricted, as observed in cells (Figure 4A), that division occurred (Fig. 4D). This was modelled as a gradual loss of individual subunits from both ends of the helix at a specified rate, such that the filament length decreases linearly in time (Movie S2, where $R_{\text{target}}/R_0 = 5\%$). In sum, these data and simulations highlight the importance of disassembling the CdvB1:CdvB2 co-polymer during constriction, so that the ESCRT-III filament doesn't crowd the neck and prevent scission.

Discussion: These findings demonstrate how proteasome-mediated degradation of CdvB, a component of the ESCRT-III ring, plays a key role in ordering the changes in ESCRT-III co-polymer structure to drive cell division, and suggests an elegant mechanism by which *S. acidocaldarius* cells divide. First, cells assemble a structural non-contractile CdvB ring at the centre of the cell. This ESCRT-III filament acts as a template for the assembly of CdvB1 and

CdvB2 ESCRT-III proteins, which have a smaller preferred radius of curvature. The tension stored in this CdvB1:CdvB2 polymer is then released once the CdvB template is removed and degraded by the proteasome, driving membrane constriction. During constriction, this co-polymer is disassembled gradually to enable scission of the membrane bridge connecting the two nascent daughter cells.

While we were able to demonstrate that the proteasome is able to directly degrade CdvB *in vitro* (Fig. S12), the process is likely more complicated *in vivo*. This is supported by the observation that a defective PAN proteasome cap leads to an accumulation of CdvB (Fig. 2C). Moreover, previous studies have implicated the ESCRT-III associated protein Vps4 (CdvC) in the division process (14, 32). In eukaryotes, Vps4 plays a role in the stepwise disassembly of composite ESCRT-III filaments, and membrane deformation (31, 33, 34). Since the role of Vps4 appears to be conserved, these data suggest that CdvC might be required to selectively extract CdvB from the composite CdvB, CdvB1:CdvB2 co-polymer. This soluble pool of CdvB would then be rapidly targeted to the proteasome via PAN, and possibly other proteins, leading to its degradation before it can be reincorporated back into the ring. While this remains speculation, under this model the degradation of CdvB would make this change in ESCRT-III polymer structure functionally irreversible. CdvC might then also catalyse the disassembly of the CdvB1:CdvB2 polymer, required to vacate the division neck, thus aiding the final process of membrane scission. In line with this idea, previous studies have found that truncating the CdvC-interacting domain in CdvB, CdvB1, or CdvB2 leads to an arrest at various points during the

constriction process (15), implying that CdvC plays one or more essential roles in archaeal cell division.

In summary, this study reveals that ESCRT-III mediated cell division in *S. acidocaldarius* is regulated by the selective proteasome-mediated degradation of CdvB. It also reveals parallels between cell cycle control in archaea and eukaryotes, implicating that proteasome-mediated regulation predate Cyclins and Cyclin-dependent kinases. Further work will be required to: i) identify all the relevant targets of the proteasome during this final cell cycle transition in archaea, ii) to determine whether the proteasome plays an analogous role in driving ESCRT-III dependent cell division in eukaryotes, iii) to determine whether the degradation of any of these proteins plays a role in resetting the archaeal cell cycle in a manner analogous the role played by Cyclin degradation in eukaryotes, and iv) to determine if there are other shared design features governing cell cycle progression across the archaeal-eukaryotic divide. However, this study emphasizes the utility of using archaea as a simple model to explore fundamental features of eukaryotic molecular cell biology that have been conserved over two billion years of evolution.

Materials and methods summary:

Cell culturing, synchronisation and drug treatments

S. acidocaldarius strains were grown at 75°C, pH 3.0-3.5, in Brock medium supplemented with NZ-amine and Sucrose, with the exception of the STK and MW001 strains that were also

supplemented with Uracil. Synchronisation was achieved with acetic acid treatment, and proteasome inhibition by supplementing bortezomib or MG132.

Biochemistry and mass spectrometry

Biochemical analyses were carried out on extracted protein and RNA by western blotting and mass spectrometry and qPCR. In vitro assays of proteasome activity were studied in the context of active and inactive proteasome assemblies and supplemented with the use of a 3xUrm1-GFP reporter. Proteins of interest were expressed *E. coli*. The antibody specificities for CdvB, CdvB1, and CdvB2 were tested by ELISA and whole western blots.

Sulfolobus genetics

Two overexpression strains were generated: 1) a dominant negative PAN-WalkerB-HA and 2) a WT CdvB2. Both proteins were subject to arabinose induction and on a plasmid complementing uracil auxotrophy.

Microscopy and flow cytometry

All microscopy and flow cytometry were done on ethanol-fixed cells, staining for DNA, the S-layer, and with antibodies against ESCRT-III homologues. For super-resolution, SRRF and linear iSIM were employed.

Crystallography

The inactive proteasome subunits were overexpressed in and purified from *E. coli*. Subsequently, crystals were grown in CZ buffer and a 3.7 Å dataset was collected from a single crystal at SOLEIL, France.

Molecular dynamics simulations

A fluid spherical membrane consisting of 48,000 particles was modelled together with the ESCRT-III filament modelled with three-beaded subunits. Simulations for the constriction and disassembly of the ESCRT-III filament were run with the LAMMPS molecular dynamics package.

References and Notes:

1. R. Bernander, The cell cycle of *Sulfolobus*. *Mol. Microbiol.* **66**, 557–562 (2007).
2. D. Ausiannikava, T. Allers, Diversity of DNA Replication in the Archaea. *Genes.* **8**, 56 (2017).
3. S. Lang, L. Huang, The *Sulfolobus solfataricus* GINS Complex Stimulates DNA Binding and Processive DNA Unwinding by Minichromosome Maintenance Helicase. *J Bacteriol.* **197**, 3409–3420 (2015).
4. Y. Caspi, C. Dekker, Dividing the Archaeal Way: The Ancient Cdv Cell-Division Machinery. *Front Microbiol.* **9** (2018), doi:10.3389/fmicb.2018.00174.
5. M. Groll, H. Brandstetter, H. Bartunik, G. Bourenkow, R. Huber, Investigations on the maturation and regulation of archaeobacterial proteasomes. *J. Mol. Biol.* **327**, 75–83 (2003).
6. J. Löwe, D. Stock, B. Jap, P. Zwickl, W. Baumeister, R. Huber, Crystal structure of the 20S proteasome from the archaeon *T. acidophilum* at 3.4 Å resolution. *Science.* **268**, 533–539 (1995).
7. F. Zhang, M. Hu, G. Tian, P. Zhang, D. Finley, P. D. Jeffrey, Y. Shi, Structural insights into the regulatory particle of the proteasome from *Methanocaldococcus jannaschii*. *Mol. Cell.* **34**, 473–484 (2009).

8. J. Maupin-Furlow, Proteasomes and protein conjugation across domains of life. *Nat. Rev. Microbiol.* **10**, 100–111 (2011).
9. J. F. Giménez-Abián, L. A. Díaz-Martínez, K. G. Wirth, C. De la Torre, D. J. Clarke, Proteasome activity is required for centromere separation independently of securin degradation in human cells. *Cell Cycle.* **4**, 1558–1560 (2005).
10. S. López-Avilés, O. Kapuy, B. Novák, F. Uhlmann, Irreversibility of mitotic exit is the consequence of systems level feedback. *Nature.* **459**, 592–595 (2009).
11. M. Glotzer, A. W. Murray, M. W. Kirschner, Cyclin is degraded by the ubiquitin pathway. *Nature.* **349**, 132–138 (1991).
12. K. Wickliffe, A. Williamson, L. Jin, M. Rape, The multiple layers of ubiquitin-dependent cell cycle control. *Chem Rev.* **109**, 1537–1548 (2009).
13. A.-C. Lindås, E. A. Karlsson, M. T. Lindgren, T. J. G. Ettema, R. Bernander, A unique cell division machinery in the Archaea. *Proc. Natl. Acad. Sci. U.S.A.* **105**, 18942–18946 (2008).
14. R. Y. Samson, T. Obita, S. M. Freund, R. L. Williams, S. D. Bell, A role for the ESCRT system in cell division in archaea. *Science.* **322**, 1710–1713 (2008).
15. J. Liu, R. Gao, C. Li, J. Ni, Z. Yang, Q. Zhang, H. Chen, Y. Shen, Functional assignment of multiple ESCRT-III homologs in cell division and budding in *Sulfolobus islandicus*: Functional assignment of multiple ESCRT-III homologs. *Molecular Microbiology.* **105**, 540–553 (2017).
16. R. S. Anjum, S. M. Bray, J. K. Blackwood, M. L. Kilkenny, M. A. Coelho, B. M. Foster, S. Li, J. A. Howard, L. Pellegrini, S.-V. Albers, M. J. Deery, N. P. Robinson, Involvement of a eukaryotic-like ubiquitin-related modifier in the proteasome pathway of the archaeon *Sulfolobus acidocaldarius*. *Nature Communications.* **6**, 8163 (2015).
17. A. Sali, T. L. Blundell, Comparative protein modelling by satisfaction of spatial restraints. *J. Mol. Biol.* **234**, 779–815 (1993).
18. J. Adams, V. J. Palombella, E. A. Sausville, J. Johnson, A. Destree, D. D. Lazarus, J. Maas, C. S. Pien, S. Prakash, P. J. Elliott, Proteasome inhibitors: a novel class of potent and effective antitumor agents. *Cancer Res.* **59**, 2615–2622 (1999).
19. D. Chen, M. Frezza, S. Schmitt, J. Kanwar, Q. P. Dou, Bortezomib as the first proteasome inhibitor anticancer drug: current status and future perspectives. *Curr Cancer Drug Targets.* **11**, 239–253 (2011).
20. X. Fu, R. Liu, I. Sanchez, C. Silva-Sanchez, N. L. Hepowit, S. Cao, S. Chen, J. Maupin-Furlow, Ubiquitin-Like Proteasome System Represents a Eukaryotic-Like Pathway for Targeted Proteolysis in Archaea. *mBio.* **7**, e00379-16 (2016).

21. N. L. Hepowitz, J. A. Maupin-Furlow, Rhodanese-Like Domain Protein UbaC and Its Role in Ubiquitin-Like Protein Modification and Sulfur Mobilization in Archaea. *Journal of Bacteriology*. **201** (2019), doi:10.1128/JB.00254-19.
22. R. Oerlemans, N. E. Franke, Y. G. Assaraf, J. Cloos, I. van Zantwijk, C. R. Berkers, G. L. Scheffer, K. Debipersad, K. Vojtekova, C. Lemos, J. W. van der Heijden, B. Ylstra, G. J. Peters, G. L. Kaspers, B. A. C. Dijkmans, R. J. Scheper, G. Jansen, Molecular basis of bortezomib resistance: proteasome subunit beta5 (PSMB5) gene mutation and overexpression of PSMB5 protein. *Blood*. **112**, 2489–2499 (2008).
23. M. Lundgren, A. Andersson, L. Chen, P. Nilsson, R. Bernander, Three replication origins in *Sulfolobus* species: synchronous initiation of chromosome replication and asynchronous termination. *Proc. Natl. Acad. Sci. U.S.A.* **101**, 7046–7051 (2004).
24. T. Gristwood, I. G. Duggin, M. Wagner, S. V. Albers, S. D. Bell, The sub-cellular localization of *Sulfolobus* DNA replication. *Nucleic Acids Res.* **40**, 5487–5496 (2012).
25. R. Y. Samson, T. Obita, B. Hodgson, M. K. Shaw, P. L.-G. Chong, R. L. Williams, S. D. Bell, Molecular and Structural Basis of ESCRT-III Recruitment to Membranes during Archaeal Cell Division. *Molecular Cell*. **41**, 186–196 (2011).
26. N. Yang, A. J. M. Driessen, Deletion of *cdvB* paralogous genes of *Sulfolobus acidocaldarius* impairs cell division. *Extremophiles*. **18**, 331–339 (2014).
27. N. Gustafsson, S. Culley, G. Ashdown, D. M. Owen, P. M. Pereira, R. Henriques, Fast live-cell conventional fluorophore nanoscopy with ImageJ through super-resolution radial fluctuations. *Nature Communications*. **7**, 12471 (2016).
28. R. Laine, K. Tosheva, N. Gustafsson, R. D. M. Gray, P. Almada, D. Albrecht, G. T. Risa, F. Hurtig, A.-C. Lindås, B. Baum, J. Mercer, C. Letierrier, P. M. Pereira, S. Culley, R. Henriques, NanoJ: a high-performance open-source super-resolution microscopy toolbox. *bioRxiv* (2018), doi:10.1101/432674.
29. S. Wold, K. Skarstad, H. B. Steen, T. Stokke, E. Boye, The initiation mass for DNA replication in *Escherichia coli* K-12 is dependent on growth rate. *EMBO J.* **13**, 2097–2102 (1994).
30. M. J. Dobro, R. Y. Samson, Z. Yu, J. McCullough, H. J. Ding, P. L.-G. Chong, S. D. Bell, G. J. Jensen, Electron cryotomography of ESCRT assemblies and dividing *Sulfolobus* cells suggests that spiraling filaments are involved in membrane scission. *Mol Biol Cell*. **24**, 2319–2327 (2013).
31. L. Harker-Kirschneck, B. Baum, A. Šarić, Changes in ESCRT-III filament geometry drive membrane remodelling and fission in silico. *BMC Biology*. **17**, 82 (2019).
32. B. E. Mierzwa, N. Chiaruttini, L. Redondo-Morata, J. Moser von Filseck, J. König, J. Larios, I. Poser, T. Müller-Reichert, S. Scheuring, A. Roux, D. W. Gerlich, Dynamic subunit turnover in ESCRT-III

- assemblies is regulated by Vps4 to mediate membrane remodelling during cytokinesis. *Nature Cell Biology*. **19**, 787–798 (2017).
33. A.-K. Pfitzner, V. Mercier, A. Roux, Vps4 triggers sequential subunit exchange in ESCRT-III polymers that drives membrane constriction and fission. *bioRxiv*, 718080 (2019).
 34. C. Caillat, S. Maity, N. Miguët, W. H. Roos, W. Weissenhorn, The role of VPS4 in ESCRT-III polymer remodeling. *Biochem. Soc. Trans.* **47**, 441–448 (2019).
 35. T. D. Brock, K. M. Brock, R. T. Belly, R. L. Weiss, Sulfolobus: a new genus of sulfur-oxidizing bacteria living at low pH and high temperature. *Arch Mikrobiol.* **84**, 54–68 (1972).
 36. M. Wagner, M. van Wolferen, A. Wagner, K. Lassak, B. H. Meyer, J. Reimann, S.-V. Albers, Versatile Genetic Tool Box for the Crenarchaeote Sulfolobus acidocaldarius. *Front. Microbiol.* **3** (2012), doi:10.3389/fmicb.2012.00214.
 37. J. Cox, M. Mann, MaxQuant enables high peptide identification rates, individualized p.p.b.-range mass accuracies and proteome-wide protein quantification. *Nature Biotechnology*. **26**, 1367–1372 (2008).
 38. S. Tyanova, T. Temu, P. Sinitcyn, A. Carlson, M. Y. Hein, T. Geiger, M. Mann, J. Cox, The Perseus computational platform for comprehensive analysis of (prote)omics data. *Nat. Methods*. **13**, 731–740 (2016).
 39. J. Schindelin, I. Arganda-Carreras, E. Frise, V. Kaynig, M. Longair, T. Pietzsch, S. Preibisch, C. Rueden, S. Saalfeld, B. Schmid, J.-Y. Tinevez, D. J. White, V. Hartenstein, K. Eliceiri, P. Tomancak, A. Cardona, Fiji: an open-source platform for biological-image analysis. *Nature Methods*. **9**, 676–682 (2012).
 40. A. G. York, P. Chandris, D. D. Nogare, J. Head, P. Wawrzusin, R. S. Fischer, A. Chitnis, H. Shroff, Instant super-resolution imaging in live cells and embryos via analog image processing. *Nat Methods*. **10**, 1122–1126 (2013).
 41. N. Kurosawa, D. W. Grogan, Homologous recombination of exogenous DNA with the Sulfolobus acidocaldarius genome: Properties and uses. *FEMS Microbiol Lett.* **253**, 141–149 (2005).
 42. A. A. Pulschen, D. R. Mutavchiev, K. N. Sebastian, J. Roubinet, M. Roubinet, G. T. Risa, M. van Wolferen, C. Roubinet, S. Culley, G. Dey, S.-V. Albers, R. Henriques, B. Baum, *bioRxiv*, in press, doi:10.1101/2020.02.18.953042.
 43. W. Kabsch, Integration, scaling, space-group assignment and post-refinement. *Acta Crystallogr D Biol Crystallogr.* **66**, 133–144 (2010).
 44. P. R. Evans, An introduction to data reduction: space-group determination, scaling and intensity statistics. *Acta Cryst D.* **67**, 282–292 (2011).

45. P. V. Afonine, R. W. Grosse-Kunstleve, N. Echols, J. J. Headd, N. W. Moriarty, M. Mustyakimov, T. C. Terwilliger, A. Urzhumtsev, P. H. Zwart, P. D. Adams, Towards automated crystallographic structure refinement with phenix.refine. *Acta Crystallogr. D Biol. Crystallogr.* **68**, 352–367 (2012).
46. A. J. McCoy, R. W. Grosse-Kunstleve, P. D. Adams, M. D. Winn, L. C. Storoni, R. J. Read, Phaser crystallographic software. *J Appl Cryst.* **40**, 658–674 (2007).
47. P. D. Adams, P. V. Afonine, G. Bunkóczi, V. B. Chen, N. Echols, J. J. Headd, L.-W. Hung, S. Jain, G. J. Kapral, R. W. Grosse Kunstleve, A. J. McCoy, N. W. Moriarty, R. D. Oeffner, R. J. Read, D. C. Richardson, J. S. Richardson, T. C. Terwilliger, P. H. Zwart, The Phenix software for automated determination of macromolecular structures. *Methods.* **55**, 94–106 (2011).
48. P. Emsley, B. Lohkamp, W. G. Scott, K. Cowtan, Features and development of Coot. *Acta Crystallogr. D Biol. Crystallogr.* **66**, 486–501 (2010).
49. B. Webb, A. Sali, *Curr Protoc Bioinformatics*, in press, doi:10.1002/cpbi.3.
50. K. Zhu, K. W. Borrelli, J. R. Greenwood, T. Day, R. Abel, R. S. Farid, E. Harder, Docking Covalent Inhibitors: A Parameter Free Approach To Pose Prediction and Scoring. *J. Chem. Inf. Model.* **54**, 1932–1940 (2014).
51. H. Yuan, C. Huang, J. Li, G. Lykotrafitis, S. Zhang, One-particle-thick, solvent-free, coarse-grained model for biological and biomimetic fluid membranes. *Phys Rev E Stat Nonlin Soft Matter Phys.* **82**, 011905 (2010).
52. S. Plimpton, Fast Parallel Algorithms for Short-Range Molecular Dynamics. *Journal of Computational Physics.* **117**, 1–19 (1995).
53. A. Stukowski, Visualization and analysis of atomistic simulation data with OVITO—the Open Visualization Tool. *Modelling Simul. Mater. Sci. Eng.* **18**, 015012 (2009).

Acknowledgments: We thank the MRC LMCB at UCL for their support; the flow cytometry STP at the F. Crick Institute for assistance, with special thanks to Sukhveer Purewal and Derek Davis; Cosetta Bertoli for mentorship and advice; Juan Manuel Garcia-Arcos for help early on in this project, the entire Baum lab for their input throughout the project; the Albers lab for advice and reagents, with special thanks to Marleen Van Wolferen and Sonja Albers; the members of the Wellcome consortium for archaeal cytoskeleton studies for advice and comments; J. Löwe, S. Oliferenko, M. Balasubramanian and D.

Gerlich for discussions and advice on the manuscript. NR and SB would like to thank Neil Rzechorzek, Aline Simon and Salman Anjum for discussion and advice. **Funding:** This work was supported by the MRC PhD scholarship award (MC_CF12266), Vetenskapsrådet (621-2013-4685), by the HFSP (LT001027/2019 fellowship) and grants from the Wellcome Trust (203276/Z/16/Z) and BBSRC (BB/K009001/1). APS is supported by the Francis Crick Institute, which receives its core funding from Cancer Research UK (FC001999), the UK Medical Research Council (FC001999), and the Wellcome Trust (FC001999). Funding also from the Isaac Newton Trust Research Grant (Trinity College and Department of Biochemistry, Cambridge) and start-up funds from the Division of Biomedical and Life Sciences (Lancaster University) to NR, and a BBSRC Doctoral Training Grant [RG53842] to SB (supervised by NR). **Author contributions:** BB and GTR conceived the study. Initial observations were made by FH and GTR. Structural work was planned and carried out by SB and NR, with assistance from MK, and LP. In vitro proteasome assays were planned and performed by DP and NR. Cell biology methods and experiments were developed by GTR, FH, GD, DM and SC with guidance from BB, RH and ACL. Molecular genetics were done by FH, DM, AAP, GTR. Biochemical analysis was carried out by FH, GTR, LM, AAP, and DPS. RNA analysis was carried out by CF, with guidance from BB and RdB. Mass spectrometry preparation and analysis was carried out by PF, CD, and GTR, with guidance from APS. The physical model was built by AH and LHK, with guidance from AS and BB. The paper was written by GTR, FH, and BB, with input from all other authors. **Competing interests:** The authors declare no competing interests. **Data and materials availability:** All data is available in the manuscript or the supplementary materials. The crystal structure of the *S acidocaldarius* 20S proteasome is available at PDB, with the ID: 6Z46. All materials are available from B. Baum or N. Robinson upon request.

Supplementary Materials:

Materials and Methods

- Supplementary Figure 1** Crystal structure of the *S. acidocaldarius* proteasome
- Supplementary Figure 2** Electron density map of the core 20S *S. acidocaldarius* proteasome
- Supplementary Figure 3** In vitro proteasome activity and sensitivity to bortezomib
- Supplementary Figure 4** Cell cycle responses to proteasomal inhibition
- Supplementary Figure 5** Proteasomal inhibition with MG132
- Supplementary Figure 6** *S. acidocaldarius* ESCRT-III homologue antibody specificities
- Supplementary Figure 7** Cdv transcript and protein level response to proteasomal inhibition
- Supplementary Figure 8** Targeted degradation of CdvB triggers constriction via CdvB1 and CdvB2
- Supplementary Figure 9** Estimation of the timeline of cell division in *S. acidocaldarius*
- Supplementary Figure 10** Degradation and disassembly dynamics of the ESCRT-III cell division ring
- Supplementary Figure 11** CdvB2 alone does not assemble into a division ring
- Supplementary Figure 12** In vitro degradation of CdvB by the 20S proteasome
- Supplementary Figure 13** Primers and plasmid for PAN-WalkerB-overexpression
- Supplementary Figure 14** Plasmid for CdvB2 overexpression
- Supplementary Table 1** Data collection and refinement statistics for the Saci_0613/Saci_0662ΔN Proteasome
- Supplementary Table 2** Mass spectrometry tables with Cdv proteins
- Supplementary Table 3** List of antibody host species and secondary antibodies
- Supplementary Table 4** List of primers used in cloning of plasmids used for protein expression
- Supplementary Table 5** List of primers used for RT-qPCR analysis
- Supplementary Table 6** List of mass spectrometry hits with bortezomib arrest and wash-out
- Supplementary Table 7** List of mass spectrometry hits with MG132 arrest
- Supplementary Movie 1** Constriction simulation without filament disassembly
- Supplementary Movie 2** Constriction simulation with filament disassembly

References (35–53)

Figure 1: *S. acidocaldarius* cell division is arrested upon inhibition of the proteasome

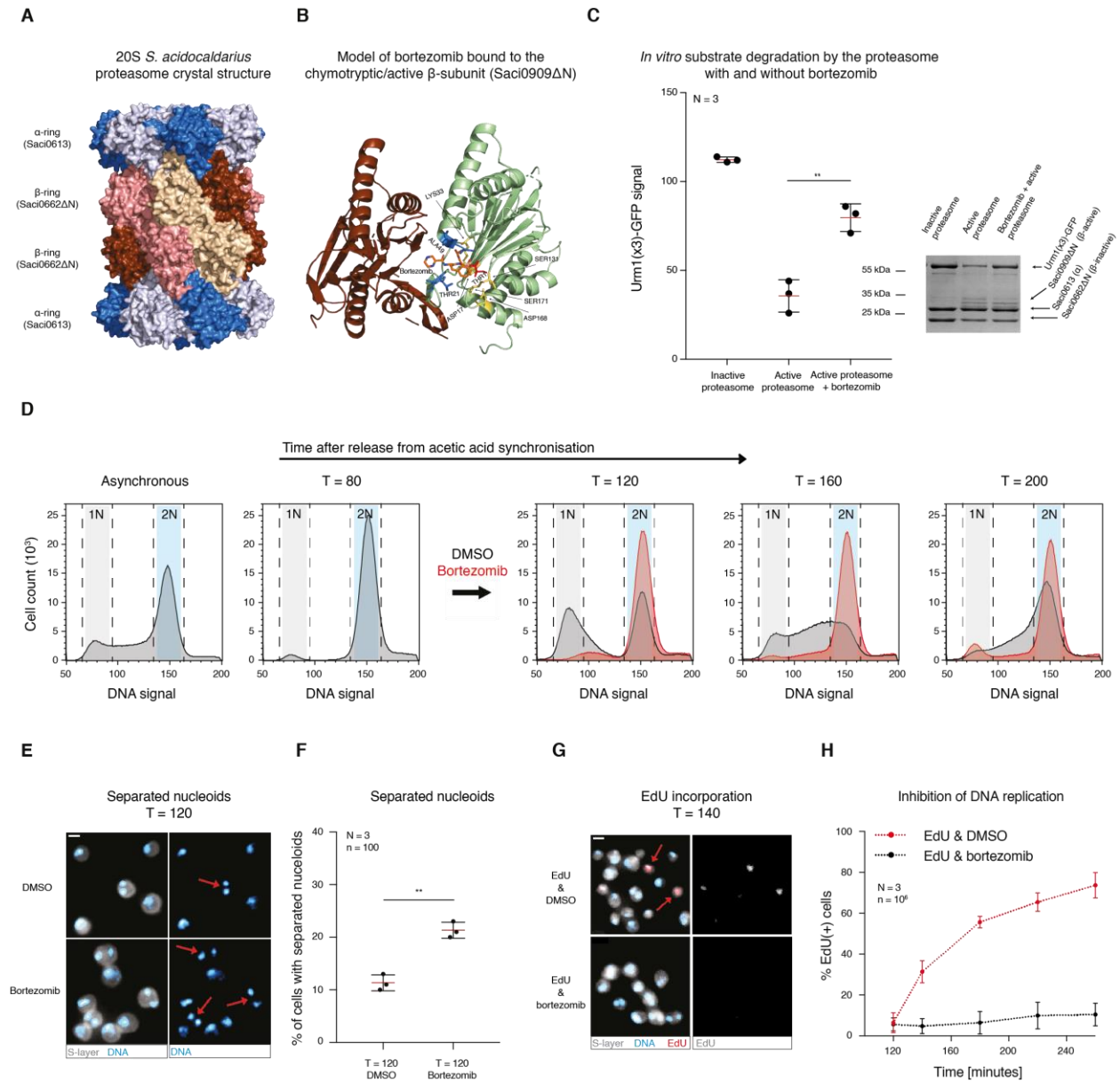


Figure 1 *S. acidocaldarius* cell division is arrested upon inhibition of the proteasome. **(A)** Side view of the *S. acidocaldarius* twenty-eight subunit Saci_0613/Saci_0662ΔN 20S proteasome assembly. Saci_0613 α-subunits are coloured alternatively dark- and light-blue and the final subunit purple [obscured – see Fig. S1]. Saci_0662ΔN β-subunits are coloured alternatively dark-red or light-red/salmon and the final subunit beige. **(B)** Modelled binding of the reversible inhibitor bortezomib to the active β-subunit (Saci_0909ΔN) chymotryptic site in the *S. acidocaldarius* 20S proteasome, using the CovDock software. The catalytic threonine (Thr1) is shown as a red stick covalently bound to the boronic acid group of the bortezomib molecule. The Asp17 and Lys33, Ser129, Asp166 and Thr169, involved in catalysis are shown as yellow sticks. The two loops (blue) harbouring the conserved residues Ala20, Ser21 and Gly47 to Val49 mediate binding of the inhibitor **(C)** Quantified degradation assay of GFP control or Urm1(x3)-GFP substrate by the Saci_0613/Saci_0662ΔN/Saci_0909ΔN 20S proteasome. Error bars represent means ± SD from N = 3. Welch's t test, p = 0.0034. **(D)** Flow cytometry histograms showing 1N and 2N DNA signal in cells in an asynchronous and a synchronised population treated with bortezomib or DMSO 80 min after release (pre-division). N = 3, n = 10⁵. Representative histograms shown. **(E)** Widefield microscopy images of synchronised cells treated with DMSO or bortezomib for 40 minutes, 80 min after release from acetic acid. Fixed cells were stained with Hoechst to visualise DNA and concanavalin A to visualise the S-layer. Red arrows indicate cells with separated nucleoids. Representative images shown. Scale bar = 1 μm. **(F)** Percentage of cells in synchronised populations harbouring separated nucleoids upon treatment with DMSO or bortezomib. Error bars represent means ± SD from N = 3, n = 100. Ratio paired t-test, p = 0.0069. **(G)** Widefield microscopy images of synchronised STK cells treated for 40 min with DMSO or bortezomib, 100 min after release from acetic acid. Staining with Hoechst for DNA, concanavalin A for the S-layer, and using “click” chemistry to visualise EdU. Red arrows indicate the cells with EdU incorporated into newly synthesized DNA. Scale bar = 1 μm. **(H)** Graph

with the percentage of synchronised cells with incorporated EdU after DMSO or bortezomib treatment.

Error bars represent means \pm SD from N = 3, n = 10⁶.

Figure 2: CdvB is targeted by the proteasome during cell division in *S. acidocaldarius*.

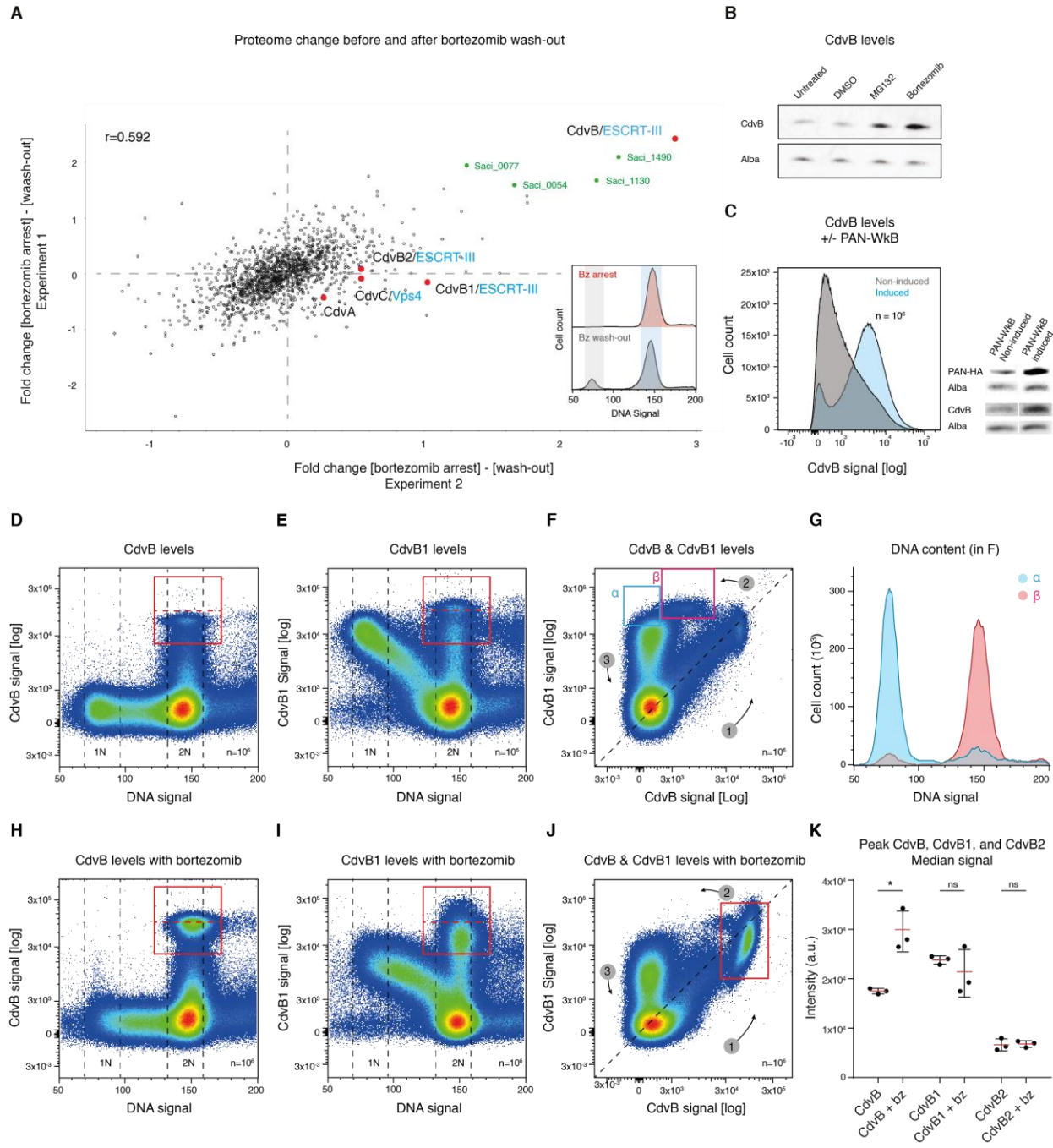


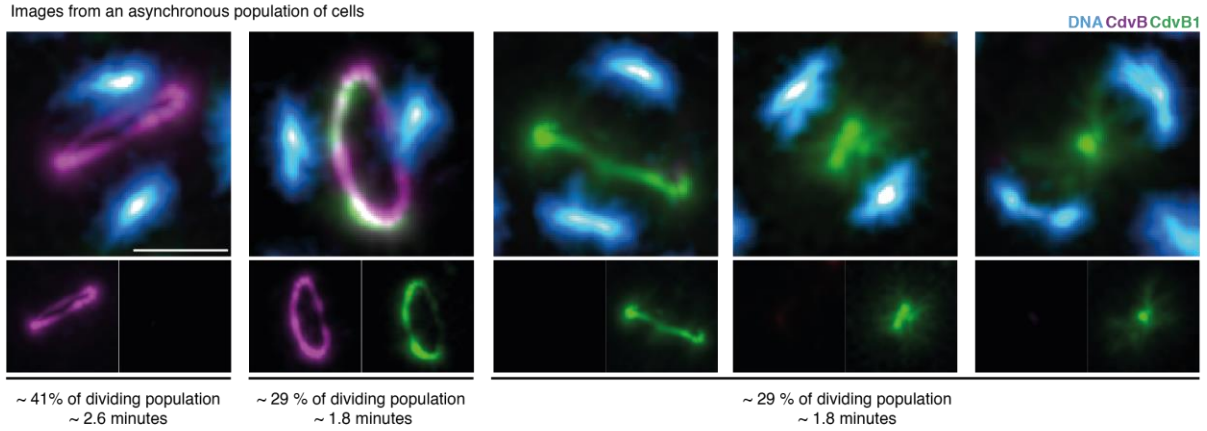
Figure 2 CdvB is targeted by the *S. acidocaldarius* proteasome during cell division. (A) Mass spectrometry scatterplot correlating two independent replicates proteome changes in (1) pre-division synchronised cells treated with bortezomib for 40 minutes vs (2) the population 15 minutes after bortezomib had been washed out (post-division). The values are the ratios of TMT intensities subtracting \log_2 transformed median normalised protein signal values in sample (2) from sample (1). The top 5 hits are in green (apart from CdvB). See Table S6 for the complete data. The insert shows two representative histograms of the bortezomib treated and wash out samples. (B) Western blots of CdvB and Alba (loading control) for synchronised cells which, 80 min after release from acetic acid, were left untreated or treated for 40 min with DMSO, MG132, or bortezomib. (C) Left, flow cytometry histogram comparing the CdvB signal under non-induced and induced conditions for a PAN-WkB-HA dominant negative overexpression strain. Right, western blots showing the change in PAN-WkB-HA and CdvB protein levels. (D, E) Flow cytometry scatterplots of DNA versus CdvB and CdvB1 protein signal of cells in an asynchronous culture. The red insert highlights the “mitotic” cells with high CdvB and CdvB1 signal respectively. Each blue spot represents a single cell, the density gradient going from blue to red. Representative plots shown, $N = 3$, $n = 10^6$. (F) Flow cytometry scatterplot of CdvB versus CdvB1 signal of an asynchronous culture showing the alternating accumulation and loss of the proteins. $N = 3$, $n = 10^6$. (G) Flow cytometry histogram of the DNA distribution of cells in the boxes shown in (F), showing the shift from 2N to 1N taking place only after complete CdvB degradation. (H, I) Flow cytometry scatterplots of DNA versus CdvB and CdvB1 signal for an asynchronous culture treated with bortezomib. Representative plots shown, $N = 3$, $n = 10^6$. (J) Scatterplot of CdvB versus CdvB1 levels in an asynchronous culture treated with bortezomib showing an accumulation of cells expressing CdvB and CdvB1, and the selective elevation of CdvB levels. Representative plot shown. $N = 3$, $n = 10^6$. (K) Quantification of median CdvB, CdvB1, and CdvB2 signal

in the mitotic populations. Ratio paired two-tailed t test for CdvB with and without bortezomib, $p = 0.0245$.

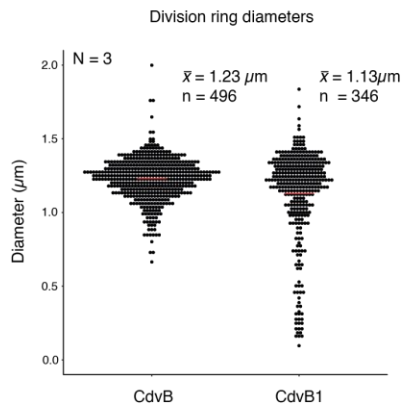
Error bars represent means \pm SD from $N = 3$.

Figure 3: Targeted degradation of CdvB triggers CdvB1/B2 ring constriction

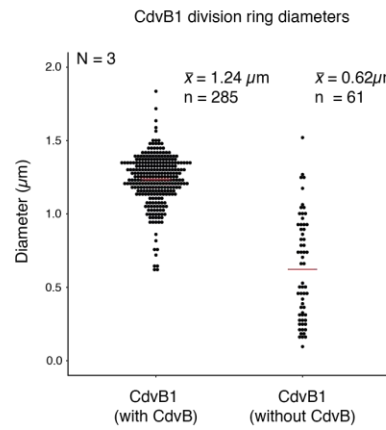
A



B



C



D

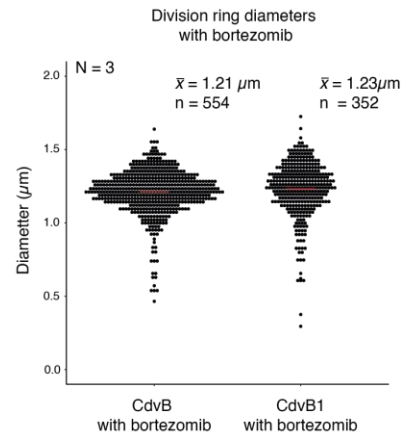


Figure 3 Targeted degradation of CdvB triggers constriction of CdvB1. (A) Representative SRRF super-resolution images of ring structures observed in exponentially growing asynchronous cell cultures using SRRF super-resolution microscopy. Cells were stained for DNA with Hoechst (blue), CdvB (purple) and CdvB1 (green), the images below the composites represent the CdvB (left) and CdvB1(right) channels. Percentages refer to the total ring bearing population. Minutes of the total cell cycle are adjusted for the exponential (binary fission) age distribution. Scale bar measures 0.5 μm . (B) Quantification of CdvB and CdvB1 ring diameters in an asynchronous culture. (C) Quantification of ring diameters of CdvB and CdvB1 in the presence and absence of a CdvB ring, showing how the removal of CdvB leads to constriction of CdvB1. (D) Quantification of ring diameters of CdvB and CdvB1 in the presence of the proteasomal inhibitor bortezomib. The data in (B), (C) and (D) all stem from more than 6 fields of view and three biological replicates. Red bars represent the mean value.

Figure 4: Model of ESCRT-III mediated cell division in archaea

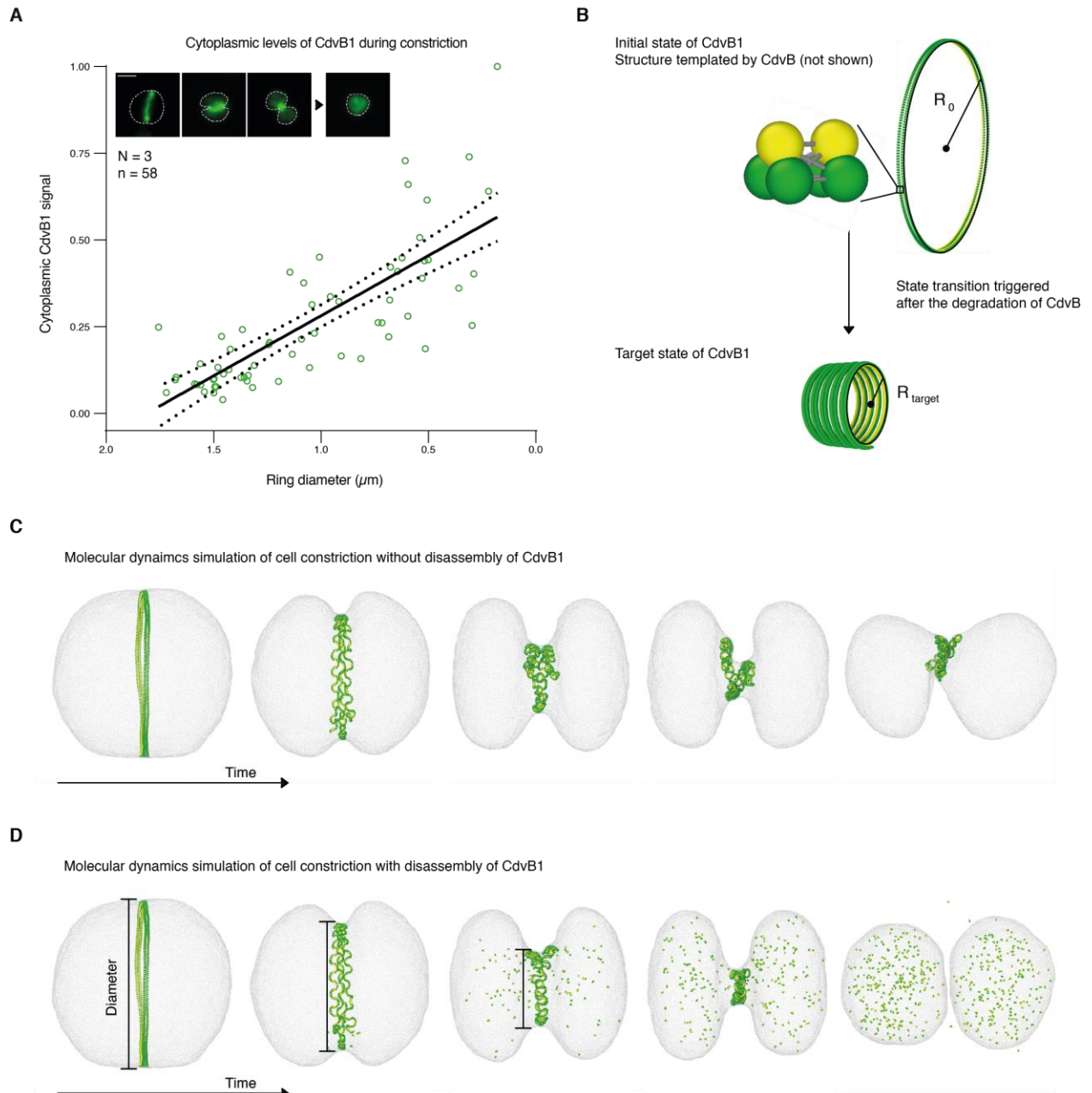


Figure 4 Physical model of ESCRT-III mediated cell division in archaea. (A) Quantification of cytoplasmic CdvB1 signal plotted against the CdvB1 ring diameter from a linear iSIM microscopy dataset; linear regression with 95% confidence interval shown in black. The insert shows representative linear iSIM microscopy images of CdvB1 at various stages of constriction and a cell in G1 after division. The outline of each cell is highlighted with the white dashed line. Scale bar = 1 μm . (B) The molecular dynamics simulation of the ESCRT-III filament is built with three-beaded subunits, which are connected by harmonic springs to form a helix. Only the green beads are attracted by the modelled cell membrane. The helix undergoes a geometrical change from a state with low curvature $1/R_0$, corresponding to CdvB1 with CdvB, to a state with high curvature $1/R_{\text{target}}$, corresponding to CdvB1 without CdvB. This change occurs after the proteasomal degradation of CdvB. (C) Simulation snapshots as a function of time showing that cell division is not achieved by constriction of the ESCRT-III filament alone; see Supplementary Movie 1. (D) Simulation snapshots showing that disassembly of the ESCRT-III filament is necessary for cell division; see Supplementary Movie 2.



Supplementary Materials for

Proteasome-mediated protein degradation resets the cell division cycle and triggers ESCRT-III-mediated cytokinesis in an archaeon.

Gabriel Tarrason Risa, Fredrik Hurtig, Sian Bray, Anne E. Hafner, Lena Harker-Kirschneck, Peter Faull, Colin Davis, Dimitra Papatziomou, Delyan R. Mutavchiev, Catherine Fan, Leticia Meneguello, Andre Arashiro Pulschen, Gautam Dey, Siân Culley, Mairi Kilkenny, Diorge P. Souza, Luca Pellegrini, Robertus A. M. de Bruin, Ricardo Henriques, Ambrosius P Snijders, Anđela Šarić, Ann-Christin Lindås, Nick Robinson and Buzz Baum

Correspondence to: b.baum@ucl.ac.uk; n.robinson2@lancaster.ac.uk

This PDF file includes:

Materials and Methods
Figs. S1 to S14
Tables S1 to S5
Captions for Movies S1 to S2

Other Supplementary Materials for this manuscript include the following:

Movies S1 to S2

Methods

Strains, culture media and growth conditions

The *S. acidocaldarius* strain DSM639 (WT)(DSMZ), MW001-CdvB2 (MW001 with the CdvB2 overexpression plasmid), and MW001-PAN-WkB-HA (MW001 with the PAN-WkB-HA overexpression plasmid) were grown at 75°C, pH 3.0-3.5, in Brock medium supplemented with 0.1% w/v NZ-amine and 0.2% w/v Sucrose (35). The mutant *S. acidocaldarius* strains MW001 (uracil auxotroph, genetic backbone) and STK (the thymidine kinase mutant) were grown at 75°C, pH 3.0-3.5, in Brock medium supplemented with 0.1% w/v NZ-amine and 0.2% w/v Sucrose and 4 µg/ml Uracil (24, 36). The optical density of liquid cell cultures was maintained at levels corresponding to exponential growth, OD600 values between 0.050 and 0.300, for between 2-12 days prior to experiments and samples were only taken within this range.

Synchronisation and drug administration

S. acidocaldarius cultures were arrested by treatment with acetic acid (final concentration 3mM) for 4.5 hours, approximately 1.5 times the doubling time (27). For *in vivo* experiments the proteasome inhibitor bortezomib was added to cells at a final concentration of 10uM, EdU to a final concentration of 200 µM, and MG132 to a final concentration of 100uM. All drugs were dissolved in DMSO and equal volumes of DMSO were used as control throughout.

Protein extraction

25 ml *S. acidocaldarius* pellets were lysed in 100-250 µl lysis buffer (TK150 buffer, supplemented with DNase1, and EDTA-free protease inhibitor cocktail, 0.1% Triton X-100). Cells were disrupted in a cup sonicator. After clarification, protein concentration was measured using a Bradford assay (Bio-Rad).

RNA extraction

TRIzol Reagent (Invitrogen) was used to isolate total RNA from 25 mL *S. acidocaldarius* pellets. The ThermoFisher trizol-reagent protocol was used for extraction. A sample clean-up was used to remove residual contaminants in which 3M Na₄OAc (1:10) and 100% ethanol (5:2) was added following RNA extraction. Samples were then incubated overnight at -20°C before washed with 75% ethanol, and spun down at 12,000 rcf at 4°C for 5 minutes. Samples were resuspended in 100µl autoclaved double-distilled water. RNA concentration and purity was measured with a NanoDrop spectrophotometer. Only samples in which the 260/280 and 260/230 absorbance ratios were approximately 2.0 were used for analysis.

Quantitative reverse transcription PCR (RT-qPCR)

The abundance of mRNA for selected genes was measured by RT-qPCR. For each reaction, 80 ng of RNA was combined with a Euroscript reverse transcriptase (Eurogentec), 2x MESA BLUE PCR reaction mix (Eurogentec) and the primer pair (Table S5) for each gene, to reach a final volume of 14 µl. Each reaction was run in triplicate and each experiment was run in three biological replicates.

RT-qPCR was run on a Bio-Rad CFX Connect Real-Time System. Each run has 39 cycles of denaturation at 95°C for 3 seconds, annealing and extension of primers at 60°C for 45 seconds, followed by measurement of fluorescence intensity. The relative fold difference RNA abundance of each gene relative to the reference gene was derived using the $2^{-\Delta\Delta C(T)}$ method for data normalisation, with equations:

$$\Delta C(T) = C(T)_{\text{GENE}} - C(T)_{\text{REFERENCE GENE}}$$

$$FD = 2^{(-\Delta\Delta C(T))}$$

C(T) indicates the number of PCR cycles required to reach a threshold in fluorescence intensity of the sample. C(T) is collected for the gene of interest and reference housekeeping gene, SecY (Saci_0574) as the average of three replicates.

ELISA

Antibody specificity was measured using 96-well Corning Costar high-binding assay plates. Plates were coated overnight at RT with 10 µg/ml bait protein and thereafter blocked for 2 hours in PBS supplemented with 1% BSA before being incubated with primary antibodies in PBST (PBS + 0.2% Tween20) for 1 hour. Secondary antibodies conjugated with HRP (ThermoFisher) were diluted according to the manufacturer's instructions into PBST before incubating for 1 hour. 1-Step™ Ultra TMB-ELISA Substrate Solution (ThermoFisher Scientific) was added for 20 minutes before being supplemented with 1 M H₂SO₄ to stop the reaction. Colorimetric signal was measured at 450 nm.

Western Blotting

Protein samples were mixed with SDS loading buffer and incubated at 99°C for 2 minutes. 8-15 µg of protein was run on NuPAGE 4-12% Bis-Tris gels (Invitrogen) at 80-120 V using MOPS running buffer. Protein was transferred to a 0.45 µm nitrocellulose membrane and stained with ponceau to visualise total protein. Blocking was done with 5% milk and PBST (PBS, 0.2% Tween20) for 1 hour. The membrane was incubated with a 5% milk-PBST mixture with primary antibodies at 4°C overnight. The membrane was washed with PBST for 15 minutes, three times, before being incubated with a 5% milk-PBST mixture with secondary antibody for 1 hour. Finally, the membrane was washed with PBST for 15 minutes, three times, before being developed using Li-COR Odyssey Infrared Imaging System. The resulting images of the blots were analysed with ImageStudioLite.

Washing out bortezomib in acetic acid synchronised cells

S. acidocaldarius cells were synchronised with acetic acid and treated with bortezomib 80 minutes after acetic acid release. After 80 minutes cells are about to divide and a 30-minute bortezomib treatment at this time leads to there being about 20-30 % of mitotic cells arrested in division. Subsequently these cells were washed twice, i.e. spun down for 6 min at 5,000rcf and resuspended in Brock media supplemented with sucrose and NZ-amine. Then, cells were incubated for 10 minutes at 75°C, before they were washed again. After this procedure the cultures were incubated at 75°C and these mitotic cells divided within 15 minutes.

Mass spectrometry sample preparation

Protein samples were generated by lysing cells in 8 M urea buffer. Equal 100 µg aliquots (as determined by Bradford protein quantification, BioRad) were stored at -80°C. Proteins were precipitated overnight in ice-cold acetone then re-suspended in 0.1 M triethylammonium bicarbonate (TEAB). Disulphide bonds were reduced by addition of 0.2 M tris(2-carboxyethyl) phosphine (incubated for 1 hour at 55 °C) and free cysteines were capped by addition of 0.4 M iodoacetamide (incubated for 30 minutes at room temperature, protected from light). Proteins were digested with 2.5 µg of trypsin (Promega, UK) overnight at 37 °C. Digestion was halted by acidification with 0.4 % trifluoroacetic acid and peptide samples were desalted using a C18 MacroSpin column (The Nest Group Inc, USA). Peptides were eluted with 80 % acetonitrile and divided to approx. 25 µg and 75 µg amounts. Both peptide solutions were dried in a vacuum centrifuge and stored at -80 °C until required. Nine samples (biological triplicates of three conditions) of dried peptides (25 µg per sample) were each solubilised in 0.05 M TEAB and labelled with one of nine TMT mass tagging reagents (Thermo Scientific) from a 0.2 mg TMT 10-plex kit. The tenth channel was used to label a pooled sample. TMT labels were removed from the freezer and thawed at room temperature for 20 minutes. Labels were solubilised (20 µl of anhydrous acetonitrile) then one sample was combined with one label. Labels are amine-reactive and modify the sample's lysine residues and peptide N-termini (one-hour incubation at room temperature). Peptide labelling efficiency was assessed by analysing an aliquot using a QExactive orbitrap (Thermo Scientific) mass spectrometer. All samples displayed > 98 % labelling efficiency so were immediately quenched (addition of 1 µl of 5 % hydroxylamine) to sequester unreacted excess label. Aliquots (5 µl) were removed from each quenched sample, combined in an Eppendorf tube and mixed thoroughly. After appropriate dilution, this mix was analysed using a QExactive orbitrap mass spectrometer to determine how much of each sample had to be combined to produce a multiplexed sample containing equal peptide amounts. A final multiplexed (10-plex) sample was produced and dried in a vacuum centrifuge. The 10-plex sample was desalted using a C18 MacroSpin column, peptides were eluted with 80 % acetonitrile and the sample was dried in a vacuum centrifuge. To improve peptide coverage and quantification depth, high pH reversed-phase fractionation column was employed. The dried sample was solubilised in 0.1 % trifluoroacetic acid, loaded onto the column (Pierce, UK) and eluted into nine separate fractions using nine elution

solutions of increasing acetonitrile percentage (initial fraction 5 %; final fraction 50 % acetonitrile). The elution solution contained triethylamine to maintain a high pH value. The nine eluted fractions were dried in a vacuum centrifuge.

Mass spectrometry

Dried peptide fractions were re-suspended in 20 μ l of 0.1% trifluoroacetic acid, sonicated for 10 minutes and centrifuged at 14,000 rpm for 3 minutes at 25°C. Each supernatant was transferred to separate glass auto-sampler vials. Single 10 μ l injections were analysed using a Fusion Lumos Tribrid orbitrap mass spectrometer coupled to an UltiMate 3000 HPLC system for on-line liquid chromatographic separation. All mass spectrometry and liquid chromatography components were sourced from Thermo Scientific, USA. The sample was loaded onto a C18 trap column (Acclaim PepMap 100; 75 μ M \times 2cm) then transferred onto a C18 reversed-phase column (PepMap RSLC; 50cm length, 75 μ m inner diameter). Peptides were eluted with a linear gradient of 2–25 % buffer B (75 % acetonitrile, 20 % water, 0.1 % formic acid, 5 % DMSO) at a flow rate of 275 nl/min over 135 minutes followed by a second linear gradient of 25–40 % buffer B over 25 minutes. MS1 instrument settings: spectra were acquired in the orbitrap at 120,000 resolution with scan range of 350–1500 m/z; maximum injection time 50 milliseconds; AGC target value 4E5; 30 % RF lens setting; 90 second dynamic exclusion. MS2 instrument settings: precursor ions with charge states $z = 2-7^+$ were selected for MS/MS higher-energy collision-induced dissociation (HCD) fragmentation; 38 % energy; acquired in the orbitrap at 60,000 resolution; maximum injection time 105 milliseconds; AGC target value 1E5.

Mass spectrometry data analysis

All data were analysed with MaxQuant software version 1.6.0.13 (37). Default TMT 10-plex quantification and identification settings were used. MS/MS spectra were searched against a UniProtKB *Sulfolobus acidocaldarius* protein database (downloaded January 2019 containing 2,222 sequences composed of 349 Swiss-Prot reviewed and 1,873 TrEMBL un-reviewed sequences) using the Andromeda search engine. Data were also searched against a reversed decoy of the protein database and a list of common protein contaminants. MaxQuant settings: trypsin enzyme (C-terminal cleavage of arginine and lysine residues); two missed cleavages; Carbamidomethylation of

cysteine as a fixed modification; N-terminal protein acetylation and methionine oxidation as variable modifications. All other MaxQuant parameters were maintained at default settings including a protein and peptide false discovery rate of 1 %. The MaxQuant output proteinGroups.txt file was opened in Perseus version 1.4.0.2 (38). Proteins were filtered to remove proteins identified in the common contaminant list and reverse decoy database. Intensity values were log 2 transformed and filtered to include only those proteins that provided intensity values in all TMT channels. Column then row data were normalised by median subtraction. Profile, volcano and scatter plots were generated for data visualisation and interpretation.

MCB9463 - TMT 6-plex analysis of bortezomib / wash out experiment.

Protein samples were generated by lysing cells in 8 M urea buffer. Equal 50 µg aliquots (Bradford quantification) were submitted to the Proteomics facility. Samples were tryptically-digested for 3 hours using the iST Sample Preparation Kit (PreOmics GmbH, Germany) following the manufacturer's instructions. Eluted peptides were dried in a vacuum centrifuge and stored at -80 °C. Six samples (biological triplicates of two conditions) of dried peptides (50 µg per sample) were solubilised in 0.05 M TEAB and labelled with one of six TMT mass tagging reagents (Thermo Scientific) from a 0.8 mg TMT 6-plex kit as described above for the TMT 10-plex kit. Labelling efficiency assessment (> 98 %), a mixing check, production of a final multiplexed (6-plex) sample, desalting and high pH fractionation were performed as described above. MS and Proteomic data analysis were also performed as described above.

Antibody generation

Protein polyclonal antibodies against CdvB1 were raised in chicken by Innovagen (Lund, Sweden) according to their standard protocol including IgY purification. The protein used for immunization, was expressed and purified from E. coli Rosetta (DE3) using Ni-affinity chromatography described in Methods. Peptide antibodies against the CdvB2 peptide NH₂-CADVNDFLRN WG-CONH₂ were raised in guinea pig by Innovagen (Lund, Sweden) according to their standard protocol including IgG purification.

Immunofluorescence labelling

Cells were fixed by stepwise addition of 4°C absolute ethanol until the concentration reached 70% from a starting point of 30% (30% - 50% - 70%). Samples were washed and rehydrated in PBS-TA (PBS supplemented with 0.2% Tween20 and 1% bovine serum albumin) before incubation overnight at 25°C with primary antibodies. Conjugated secondary antibodies were used for detection of the target proteins (Table S3). The S-layer was stained by incubating the rehydrated sample with 200 µg/ml Concanavalin A conjugated to Alexa Fluor 647 (ThermoFisher, C21421) for 3-5 hours. DNA was visualized by the addition of 1 µg/ml Hoechst (Invitrogen Cat, H3570) to samples after final washes. EdU was labelled via Click-IT chemistry according to kit instructions (ThermoFisher, C10639).

Microscopy

Microscopy samples were prepared by coating LabTek chambered slides with 2% polyethyleneimine (PEI) for 30 minutes at 30°C. Slides were then washed with distilled water, and 200 µl of stained cell suspension was added and spun down onto the slides for 30 minutes at 1000 RCF in a swing-bucket rotor. Super-resolution was achieved using the NanoJ liveSRRF package for Fiji (27, 28, 39). Images were captured for 1 second in 100 x 10 µs intervals on a Nikon Ti2, 1.49NA, 100x objective (Nikon CFI Apochromat TIRF 100XC oil objective) with a Photometrics Prime 95B sCMOS camera. Illumination was provided with a CoolLED pE-4000 LED illuminator. Analysis of ring diameters and nucleoid segregation was done with the ObjectJ plugin for Fiji (sils.fnwi.uva.nl/bcb/objectj/). Data was gathered from 3 biological replicates. The iSIM (40), VisiTech, and widefield microscopy was completed on a Nikon Ti, 1.45NA, 100x objective (Plan Apo λ 100x oil) with an ORCA-Flash4.0 V3 Digital CMOS or SID4Bio camera respectively.

Flow cytometry

Flow cytometry analysis was carried out on BD-Biosciences LSR II and BD-Biosciences Fortessa with immunostained cells going through the following lasers and filters: lasers: 355nm, 488nm, 561nm 633nm filters: 450/50UV, 525/50 Blue, 582/15 YG, 710/50 Red. Side Scatter and Forward scatter was also recorded. Analysis was carried out on FlowJo software v10.

Protein cloning, expression, purification for antibody verification

CdvB, CdvB1 and CdvB2 genes were amplified from genomic *S. acidocaldarius* DNA with Phusion polymerase (NEB) according to the manufacturer's instructions. The primers used in this study can be found in Table S5 and carried homologous regions to the pSUMO-YHRC plasmid (Addgene 54336). For plasmid construction the Gibson Assembly (NEB) was used according to the manufacturer's instructions. A 2000 ml culture of *E. coli* Rosetta (DE3) transformed with pSUMO_S1373 (CdvB), pSUMO_S0451 (CdvB1), or pSUMO_1416 (CdvB2) was cultivated in LB media supplemented with 0.1% D-glucose, 50 µg/ml Kanamycin and 34 µg/ml Chloramphenicol at 37°C until OD₆₀₀ reached 1.5. Following 30 minutes incubation at 4°C, expression was induced with the addition of 0.5 mM IPTG overnight. Cells were harvested and resuspended in Buffer A (50 mM Tris pH 7.5, 500 mM NaCl, 5% Glycerol) supplemented with 20 mM imidazole before being lysed on ice through sonication. The lysate was heat-inactivated at 70°C for 20 minutes before debris was pelleted at 20,000 RCF for 45 minutes. The supernatant was loaded onto an equilibrated His GraviTrap (GE Healthcare). The loaded column was washed with 15 ml Buffer A supplemented with 20 mM imidazole before being eluted with Buffer A supplemented with 250 mM imidazole. Fractions were loaded onto a PD10 Salt Exchange Column (GE Healthcare) equilibrated with Buffer A. Protein bearing fractions were supplemented with Ulp1 and left at RT overnight to cleave the sumo-tag. Sample were added to a His GraviTrap equilibrated with Buffer A, collecting the elute. Aliquots were snap-frozen in liquid nitrogen and stored at -80°C.

Overexpression of PAN-WkB-HA

For PAN-WkB-HA overexpression, a synthetic gene containing restriction sites (PciI and XhoI) flanking the *PAN* gene with a WalkerB point mutation [E237Q] (Saci_0656-WkB) was made (Thermo Scientific®) (Fig. S12A). The gene was inserted via digestion and ligation into a pSVAaraHA-stop plasmid containing an arabinose-inducible promoter and HA tag. This was done by digesting the synthetic gene construct with PciI and XhoI, and the plasmid with NcoI and XhoI, followed by ligation. Thus, we created the plasmid pSVA-araFX-PAN-WkB-HA (Fig. S13B). The plasmid was then methylated *in vivo* by transforming the plasmid constructs into *E. coli* ER1821 (New England Biolabs) (41).

These methylated plasmids were then used to transform MW001 competent cells and positive colonies were selected using gelrite-Brock plates, following established practice in *Sulfolobus* genetics (36).

Overexpression of CdvB2

For CdvB2 overexpression, a synthetic gene containing restriction sites (NcoI and XhoI) flanking the *cdvB2* gene (Saci_1416) was made (Thermo Scientific®) (Fig. S13A). The gene was inserted via digestion and ligation into a plasmid (pSVAaraFX-stop) containing an arabinose-inducible promoter, following the procedure as previously reported (42). Thus, we created the plasmid pSVA-araFX-CdvB2 (Fig. S13B). The plasmid was then methylated *in vivo* by transforming the plasmid constructs into *E. coli* ER1821 (New England Biolabs) (43). These methylated plasmids were then used to transform MW001 competent cells and positive colonies were selected using gelrite-Brock plates, following established practice in *Sulfolobus* genetics (36).

Crystallization of the Saci0613/Saci0662ΔN 20S core proteasome

The inactive Saci0613/Saci0662ΔN proteasome was overexpressed in *E. coli* and purified via heat treatment at 70°C in CR buffer (100 mM Tris-HCl pH 8, 300 mM NaCl, 10% glycerol). Stable proteasome complexes were retrieved from the supernatant using Nickel-agarose IMAC chromatography and eluted in CR buffer supplemented with 500 mM imidazole. The complex was further purified by two subsequent rounds of size exclusion chromatography in GF buffer (150 mM NaCl, 20 mM Tris pH 8.0, 5% glycerol) using a Superdex 200 10/300 GL gel filtration column. Elution fractions corresponding to fully formed proteasomes (four stacks of homo-heptameric toroids) was then concentrated to 10 mg/ml. Crystals were grown using equal volumes of CZ buffer (25% PEG 1500, 0.1M MMT buffer pH5 [200 mM DL-malic acid, 400 mM MES, 400 mM Trizma]) and 10 mg/ml Saci0613/Saci0662ΔN complex. The initial 0.6 ml drops were equilibrated against a 70 ml well and the crystals generated were then used to seed 2 ml drops equilibrated against a 60 ml well, to increase the size and resolution of the crystals. Crystals were transferred to a drop of CZ solution supplemented with 30% glycerol and immediately snap frozen in liquid nitrogen. The 3.7 Å dataset was collected from a single crystal at SOLEIL (proxima 2 beamline) France at a wavelength of 0.9801 nm.

The data were integrated using XDS (43). The space group symmetry was assigned in POINTLESS and intensities were scaled in AIMLESS (44). Molecular replacement and automated refinement were carried out in PHENIX (45-47). Manual refinement was carried out using COOT (48).

Modelling of the Saci_0909ΔN catalytically active β-subunit

A homology model of the active Saci_0909ΔN β subunit was generated with Modeller 9.20 (49) using the crystallographically determined structure of the inactive Saci_0662ΔN β subunit. To position the catalytic threonine correctly the structures of *Archaeoglobus fulgidus* (PDB ID code 1J2Q) and *Saccharomyces cerevisiae* (PDB ID code 4NNN) were also incorporated as templates. The final model was determined by its discrete optimised protein energy (DOPE) score.

Docking of MG132 and bortezomib

A docking model for bortezomib was generated in CovDock (50) using only the Saci_0909ΔN/Saci_0662ΔN pair of subunits that form the substrate binding pocket and receptor. The catalytic threonine of Saci_0909ΔN was identified for covalent attachment to the boronic acid moiety of the bortezomib proteasome inhibitor. Final models were chosen based on a combination of docking energy scores (kcal / mol) prior to the formation of the covalent bond and visual inspection to check for correspondence with the experimentally determined binding state of bortezomib in the *Saccharomyces cerevisiae* 20S proteasome (PDB ID: 2F16 and 4QVW).

***In vitro* 20S proteasome processing assays with bortezomib inhibition.**

The 20S proteasome core proteasome degradation reactions were performed as described previously (16). 10 μg of the GFP, or 3xUrm1-GFP, was incubated with 30 μg 20S proteasome complex in reaction buffer (20 mM Tris acetate (pH 8.0), 100 mM NaCl, 5 mM MnCl₂, 10 mM MgOAc, 50 mM KOAc, 1 mM Zn(OAc)₂, 5% glycerol and 0.02% β-mercaptoethanol) in a 75 μl reaction volume at 63°C for 0, 60, 90, or 120 min, respectively. Bortezomib (solubilized in DMSO as a 100 mM stock) was added to the appropriate reactions at a final concentration of 50 μM, 3.3 μM, 1.7 μM

or 0.8 μ M. After addition of 2X Laemmli protein loading buffer, the products were then separated by SDS-PAGE, and visualized with Coomassie stain.

***In vitro* 20S proteasome processing assay with the bortezomib-insensitive mutant.**

The bortezomib-insensitive Saci0909V49T mutant construct was generated from the Saci0909 Δ N clone by site-directed mutagenesis (QuikChange, Agilent) using the primer Saci0909 Δ NV49T (GGATTACGACTGCAGGTAGCacTGCTGATTTACAATTTATATATGAAGC). Upon co-transformation with the Saci_0613 and Saci_0662 Δ N plasmids in rosetta cells, the Saci_0613/Saci_0662 Δ N/Saci_0909 Δ NV49T bortezomib resistant proteasome was expressed and purified as described above and used under the same experimental conditions as the non-mutated 'wild-type' 20S proteasome complex.

***In vitro* 20S proteasome processing assay of CdvB, with and without bortezomib**

The *S. acidocaldarius* CdvB protein was purified with modifications for proteasomal processing assays. The recombinant plasmid pSUMO_S1373 was transformed in *E. coli* Rosetta(DE3)pLysS strain (Novagen), protein expression was induced at mid-log phase by the addition of 0.4 mM IPTG, and cells were incubated for 3 hours at 37 °C. Cells were then harvested by centrifugation, resuspended in 50 mM Tris-HCl pH 7.5, 300 mM NaCl, 25 mM imidazole and 5 % (v/v) glycerol, lysed using French Press and clarified by centrifugation. The soluble fraction was loaded into a Histrap HP 1mL column (GE Healthcare) and the recombinant protein was eluted by the addition of the same buffer used for cell resuspension supplemented with 250 mM imidazole. The N-terminal His6-SUMO tag was removed incubating with Ulp1 SUMO protease overnight at 4°C. Finally, CdvB was purified by size exclusion chromatography using a Hiloal 16/600 Superdex 75 pg column (GE Healthcare) equilibrated with 50 mM Tris-HCl pH 7.5, 300 mM NaCl and 5 % (v/v) glycerol. Protein content was analysed by SDS-PAGE and Imperial protein staining (Thermo Scientific) and concentration was determined using the BCA assay reaction kit (Pierce). Degradation by the 20S proteasome *in vitro* was conducted under the same experimental conditions as the non-mutated 'wild-type' 20S proteasome complex.

Coarse-grained molecular dynamics simulations

Following the notation from Yuan et al. (51), we modelled a fluid, spherical membrane consisting of 48,000 particles with interaction parameters $\epsilon_{\text{bead-bead}} = 4.34 k_B T$, $\xi = 4$, $\mu = 3$, and $r_{\text{cut}} = 1.12 \sigma$, where σ is the membrane particle diameter which roughly corresponds to 10 nm in our simulations.

The ESCRT-III filament is simulated using the model developed by Harker-Kirschneck et al. (31). The filament consists of three-beaded rigid subunits (see inset in Fig. 4B) which are connected to each other via the same set of nine strong harmonic bonds (bond strength $K = 600 k_B T$). Because the resting bond lengths between subunits are the same throughout the filament, they define what shape the filament will adopt when at rest. They are chosen so that the filament possesses an intrinsic 3D curvature and hence forms a ring in its rest state with target radius R_{target} . By varying the bond lengths, we can vary the target radius and form larger and smaller filament helices. The green beads of the filament are attracted to membrane beads at a distance r_{ij} via a Lennard-Jones potential:

$E_{ij} = 4 \epsilon ((\sigma/r_{ij})^{12} - (\sigma/r_{ij})^6)$, for $r_{ij} < r_c$, with $\epsilon = 4 k_B T$, $\sigma = 10 \text{ nm}$ and $r_c = 11.2 \text{ nm}$. The yellow filament beads only interact with the membrane via volume exclusion (meaning they can't overlap with, but are not attracted to, the membrane). Volume exclusion also applies to subunits within the filament interacting with each other.

In order to investigate how the constriction and disassembly of the ESCRT-III filament affects the cell membrane dynamics, we ran our simulations with the Molecular Dynamics package LAMMPS (<https://lammps.sandia.gov/>) (52). All particles in the system experience Langevin dynamics with friction coefficient $\gamma = m / t_0$ set to unity, where m is the particle mass (set to unity for all particles) and t_0 is the simulation unit of time. The filament starts off in the the CdvB1(CdvB+) state in which it has a low curvature (large initial radius R_0 resembling the cell radius). We first equilibrate the system for 2×10^5 time-steps (with a fixed time-step of $0.01 t_0$, where t_0 is the molecular dynamics unit of time), to ensure that the ESCRT-III filament attaches to the membrane.

We then model the state after CdvB degradation by reducing the radius of the filament by 95% ($R_{\text{target}}/R_0 = 5\%$), while keeping it attached to the membrane (entering the CdvB1(CdvB-) state). This is done by adjusting the resting bond lengths of the filament to a smaller target radius, and it happens instantaneously, meaning all bonds within the filament are adjusted at the same time.

In the simulation that includes disassembly, we then begin to disassemble the filament by removing individual subunits from both ends of the helix by turning their bond strengths to 0 (bond strength $K = 0 k_B T$). Every 2000 time steps two bonds are removed, making the disassembly rate $\lambda = 2/(20 t_0)$. Consequently, the filament length $N(t) = N_0 - \lambda t$ decreases linearly in time. For simplicity the filament length $N(t)$ is defined as the number of subunits that is still integrated in the filament at time t .

This process continues until the last subunit of the ESCRT-III filament is disassembled. After that the simulation equilibrates for another 10^6 time-steps. In the simulation without the disassembly the filament equilibrates for 10^7 time-steps right after the instantaneous curvature change. The simulation results are then visualized by the open-source software OVITO (53).

Stochastic sampling method for CdvB degradation

The data suggests that rapid degradation of CdvB is key to cell division. In order to investigate how quickly the initial CdvB level is degraded in time, we use a simple stochastic sampling method. For that purpose, we assume that the CdvB level of each individual cell follows a power law with intrinsic exponent α . Based on that we sample CdvB levels for an ensemble of cells that are stochastically distributed in time (i.e. an asynchronous exponentially growing population). This computational procedure agrees with the experimental measurements shown Fig S10C. Consequently, by varying the model exponent α and comparing the result to experiments we can determine which α best fits the experimental data and thus find how quickly CdvB is degraded prior to cell division.

A power law was assumed for how the initial CdvB level degrades over time, i.e. $L(t) = L_0 - r * t^\alpha$. L_0 is the initial CdvB level that follows a Gaussian distribution according to the data in the peak CdvB-CdvB1 population in asynchronous cell populations. The constant associated to the speed of the process, r , was assumed to be fixed for all the cells. We defined it as $r = (L_i - L_f) / (T^\alpha)$, where it is assumed that L_i is the largest value measured and L_f is the smallest value measured, and T is the time that the whole process took to finish. Alpha is the exponent of the power law.

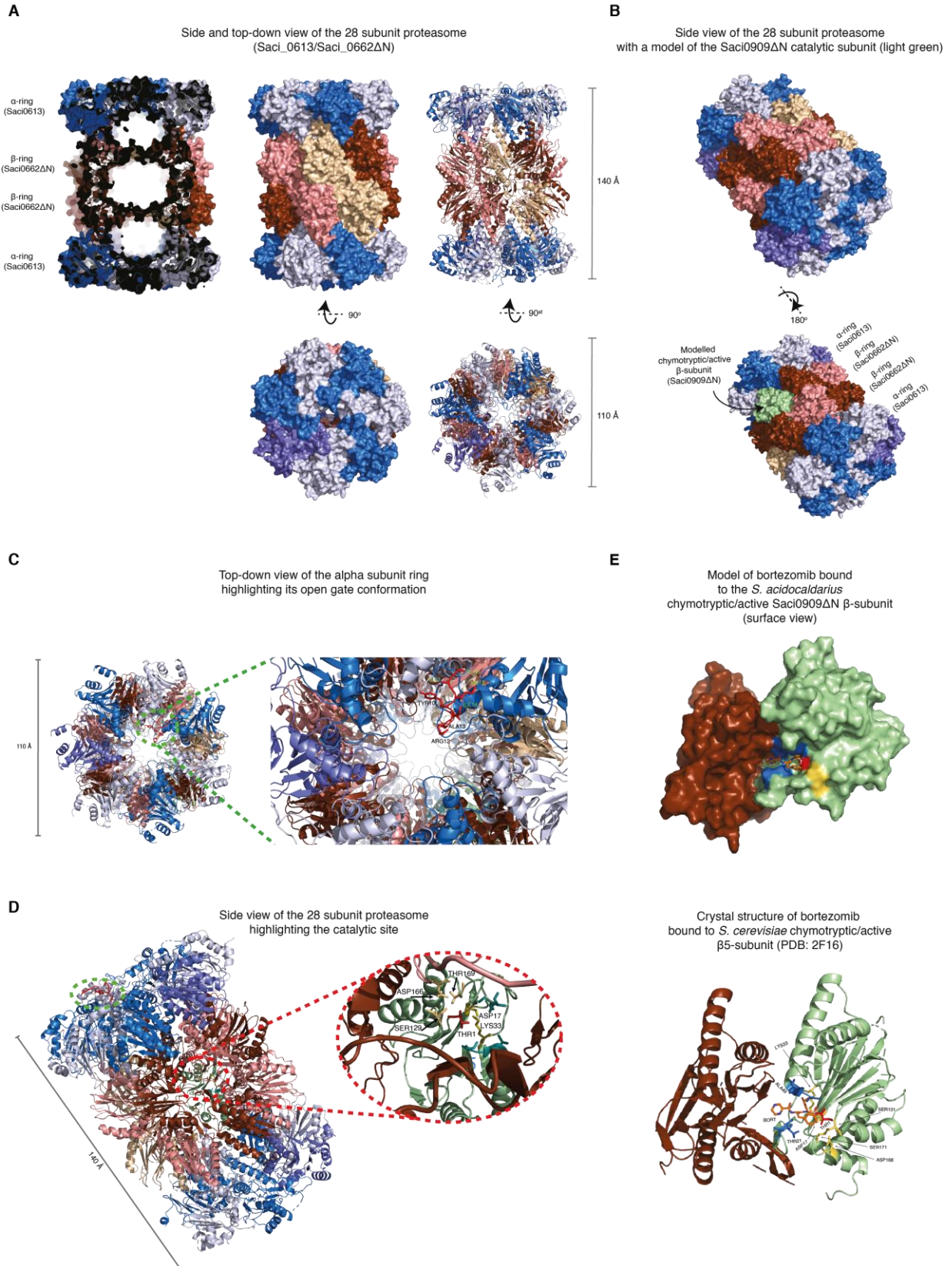
For the sampling, a random number was chosen for the initial value L_0 according to the Gaussian distribution and another random number for the time t at which the CdvB level in a specific cell is measured. That time is uniformly distributed over $[s * \text{lifetime}; \text{lifetime}]$, where $s < 1$ indicates the start of the measurement. $\text{lifetime} = ((L_0 - L_f) / r)^{(1/\alpha)}$ is the time it would take to degrade an initial random level L_0 to the final value L_f , please note this is an approximation given that L_f is fixed for all cells. Also, please note that the measurements end before CdvB is fully degraded, i.e. lifetime is not the time to reach $L(t) = 0$ but to reach $L(t) = L_f$, and that the measurements start not at time $t = 0$ but at time $t = s * \text{lifetime}$. This is in line with the data, as the degrading CdvB population does not reach a zero level. A cell's specific CdvB level is then estimated to be $L(t) = L_0 - r * t^\alpha$ and that value then stored. This process is repeated 7292 times, for as many cells as there are in the population called degrading CdvB, and the results are then sorted in descending order.

The above procedure was completed for different combinations of the parameters alpha and s and compared to the result to the experimental data. From that, $\alpha = 0.22$ and $s = 0.12$ came close to the experimental data. The fact that the scaling exponent α is small (substantially smaller than one) confirms that CdvB degrades quickly in the beginning of the division process to trigger constriction.

Statistical analysis

All statistical analysis and data processing were done using Microsoft Excel or GraphPad Prism 6 software. Significance was defined as $p < 0.05$. Significance levels used were * $P < 0.05$, ** $P < 0.01$, *** $P < 0.001$ and **** $P < 0.0001$.

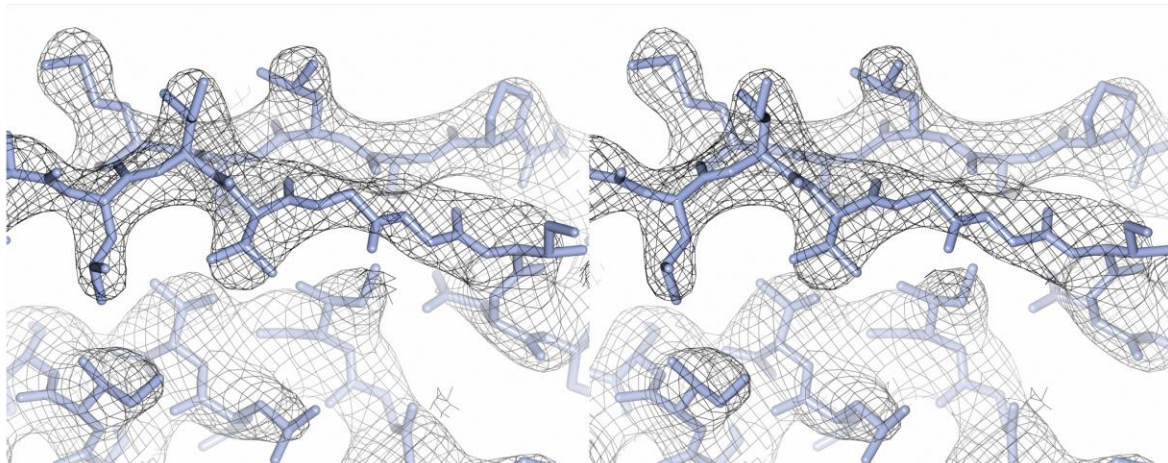
Supplementary Figure 1 Crystal structure of the *S. acidocaldarius* proteasome



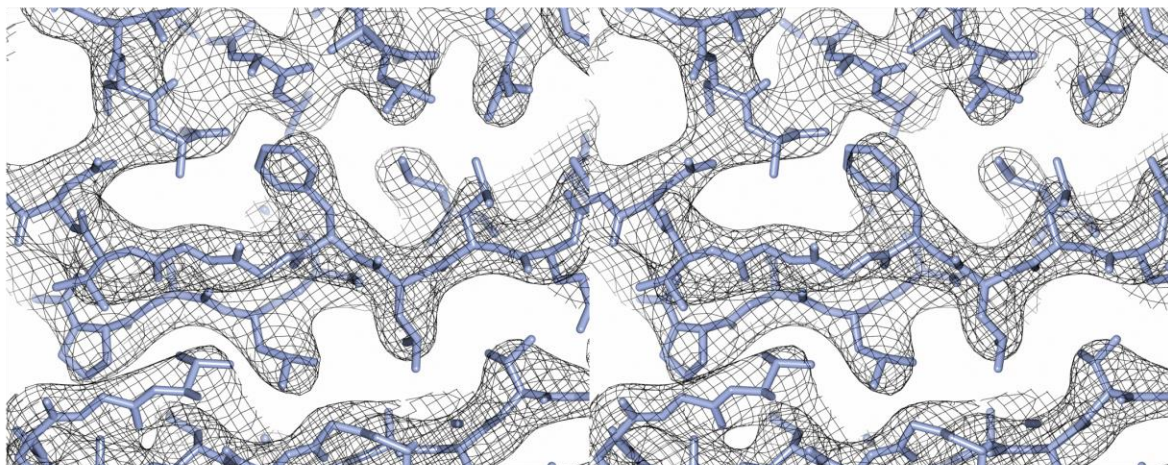
Supplementary Figure 1 Crystal structure of the *S. acidocaldarius* proteasome. (A) (top) Side view of the *S. acidocaldarius* twenty-eight subunit Saci_0613/Saci_0662ΔN 20S proteasome assembly. (bottom) The 20S barrel rotated through 90° to provide a top-down view of the structure highlighting the 'open' entrance pores and the translocation channel passing through all three chambers. Saci_0613 α-subunits are coloured alternatively dark-, light-blue and the final subunit purple. Saci_0662ΔN β-subunits are coloured alternatively dark-red, light-red and the final subunit beige. (B) Side view of the 20S proteasome assembly, with the modelled Saci_0909ΔN catalytic subunit (light green) inserted into the Saci_0613/Saci_0662ΔN 20S crystal structure. (C) Top-down view of the *S. acidocaldarius* twenty-eight subunit Saci0613/Saci0662ΔN 20S proteasome assembly, including the modelled Saci909ΔN active subunit, highlighting the 'open' conformation of the alpha-subunit gating. The outer rings are formed from a homo- heptameric arrangement of Saci0613 alpha-subunits, which are coloured purple and then alternately marine-blue and light-blue. The Saci0662ΔN beta-subunits of the inner rings are coloured alternately dark-red, light red and the final subunit beige. The extended region of α-subunit-1 residues 6-14 (AAMGYDRAI) (highlighted by the green-dashed circle) is coloured red and the side chains of these residues are shown as sticks. (right) magnified view of the pore region, highlighting the additional residues 6-14 (AAMGYDRAI) that could be built into the density map at the N-terminus of α- subunit-1. (D) Side view of the 20S proteasome assembly with the extended region of α-subunit-1 residues 6-14 (AAMGYDRAI) highlighted by the green-dashed circle. Note the modelled Saci909ΔN active subunit (green) is on the opposing side of the beta-ring. (right) Magnified view through the Saci0662ΔN beta-ring, with a cutaway to reveal the modelled Saci909ΔN active subunit (green) and the key catalytic residues (Thr1, Asp17 and Lys33) at the active site, with three further conserved residues (Ser129, Asp166 and Thr169), which are thought to aid catalysis and maintain the structure of the active site. (E) Modelled binding of the reversible inhibitor bortezomib to the Saci_0909ΔN chymotryptic site in the *S. acidocaldarius* 20S proteasome, using the CovDock software. Surface view (top) of the bortezomib inhibitor (orange sticks) covalently attached to the active site threonine (Thr1), shown as a red stick covalently bound to boronic acid group of the bortezomib molecule. (bottom) Crystal structure (PDB:2F16) of bortezomib binding at the *S. cerevisiae* 20S proteasome focusing on substrate binding pocket formed between the β5 chymotryptic β-subunit (light green) and adjacent β-subunit (brown).

Supplementary Figure 2 Electron density map of the core 20S *S. acidocaldarius* proteasome

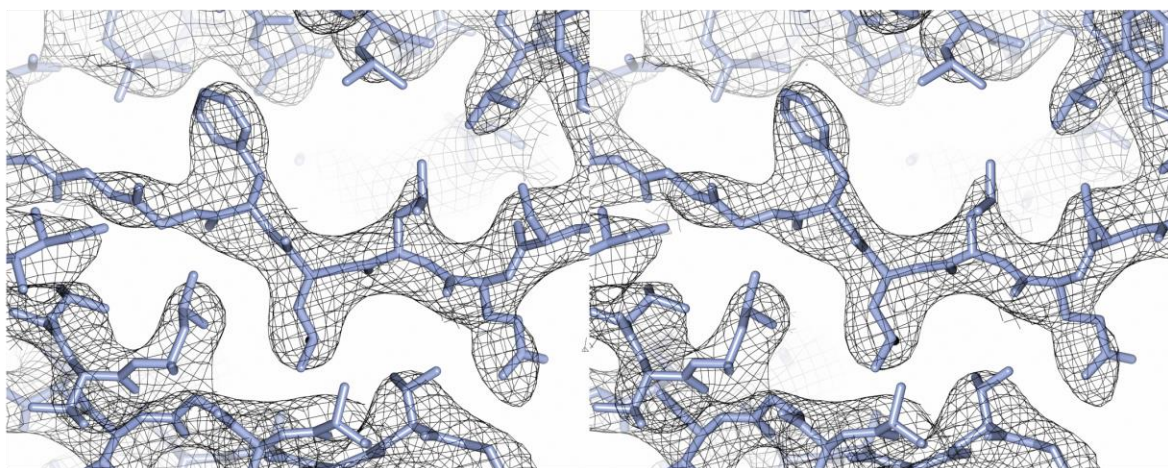
A



B

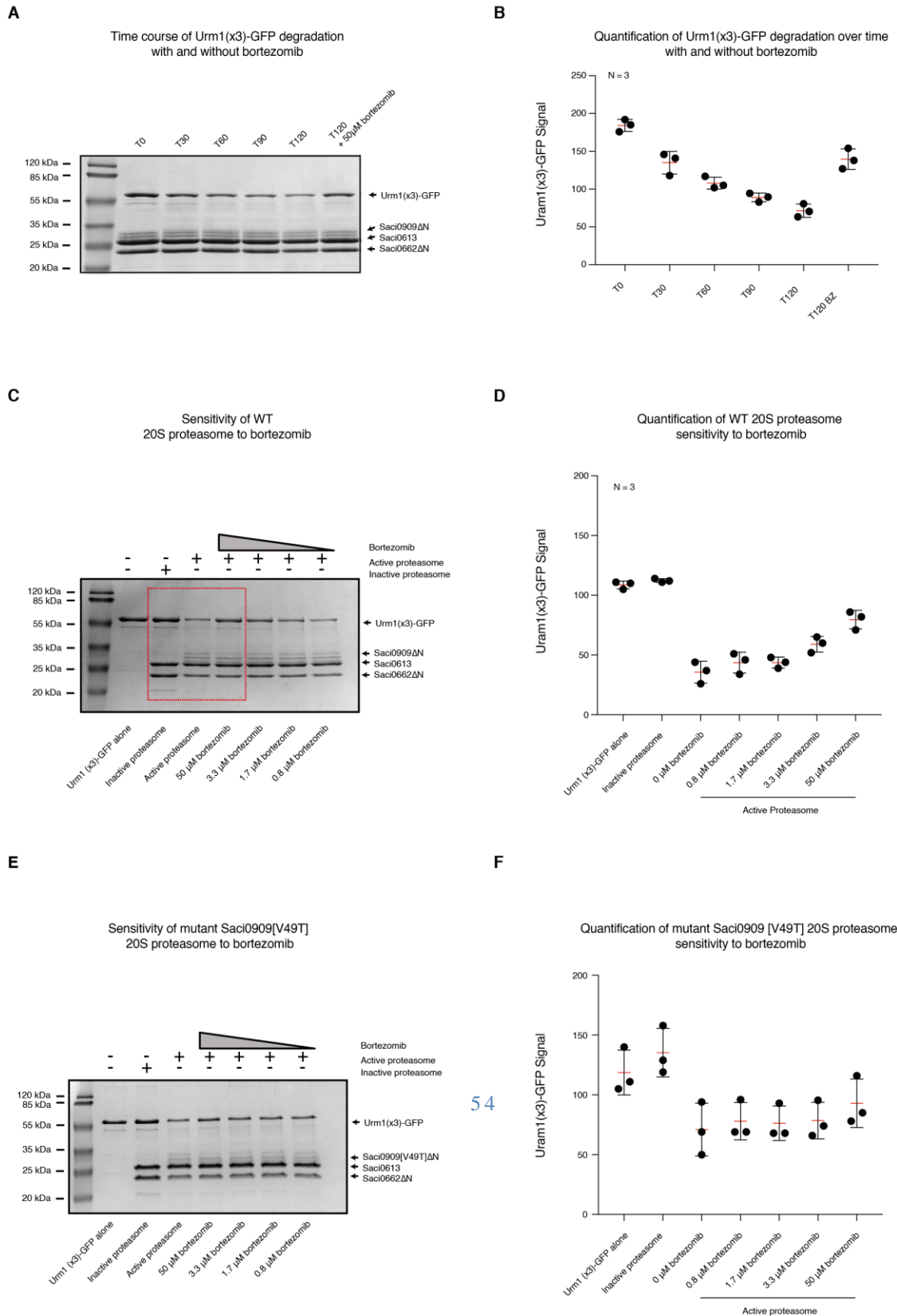


C



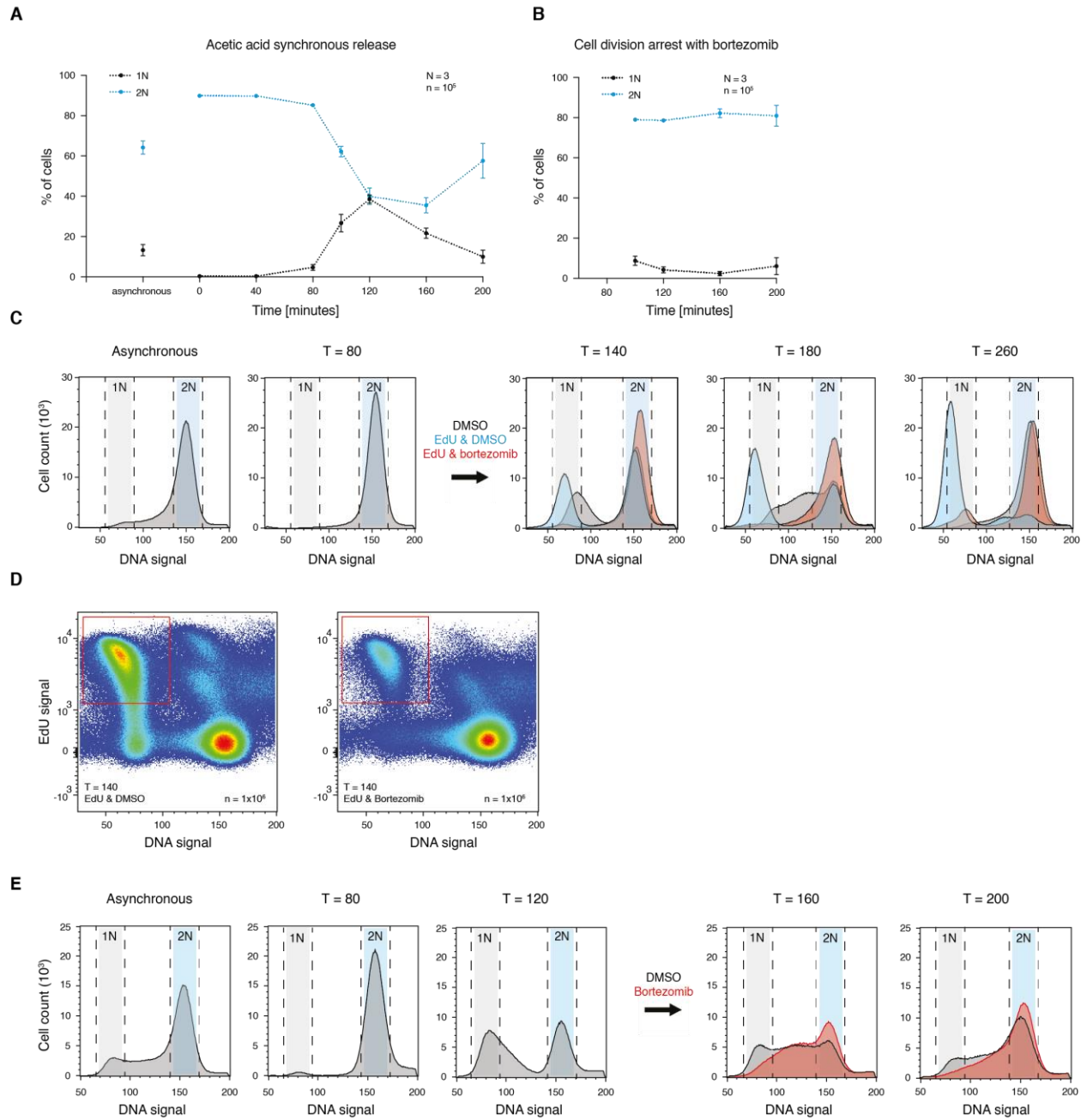
Supplementary Figure 2 Electron density map of the core 20S *S. acidocaldarius* proteasome. Stereo image of a portion of the electron density map of the *S. acidocaldarius* Saci_0613/Saci_0662ΔN proteasome structure [Type of map: mtz, Contour level: 1 sigma]. **(A)** Segments from subunit B secondary structure element α -3. **(B)** subunit B secondary structure element β -5. **(C)** subunit a secondary structure element β -6.

Supplementary Figure 3 In vitro proteasome activity and sensitivity to bortezomib



Supplementary Figure 3 In vitro activity and sensitivity of the 20S *S. acidocaldarius* proteasome to bortezomib. (A) Time course of a 20S proteasome assay with Saci_0613/Saci_0662ΔN/Saci_0909ΔN using 3xUrm1-GFP substrate. 10 μg of 3xUrm1-GFP substrate was incubated with 30 μg of the active proteasome complex for 0, 30, 60, 90 or 120 minutes at 63°C. In the last lane 3xUrm1-GFP is incubated with the 20S proteasome for 120 minutes at 63°C, but also with 50 μM bortezomib inhibitor. (B) Quantification of the 20S proteasome time course assay showing the degradation of Urm1(x3)-GFP signal over time. Error bars represent means ± SD from N = 3. (C) 20S proteasome bortezomib sensitivity assay using 3xUrm1-GFP substrate. 10 μg of 3xUrm1-GFP substrate was incubated with 30 μg of the active proteasome complex in conditions with 50 μM, 3.3 μM, 1.7 μM and 0.8 μM bortezomib at 63°C. 3xUrm1-GFP substrate degradation activity of an inactive 20S proteasome assembly made up of Saci_0613/Saci_0662ΔN was used as a negative control. The Saci_0613/Saci_0662ΔN/ Saci_0909ΔN active 20S proteasome assembly was also used in the absence of the inhibitor as a positive control. The red dashed-box region indicates the sections of the gel that are presented in Figure 1C in the main text. (D) Quantification of the 20S proteasome bortezomib sensitivity assay, showing Urm1(x3)-GFP degradation when incubated with different concentrations of bortezomib. Error bars represent means ± SD from N = 3. (E) The same experimental conditions as in (C) carried out with a mutant β active subunit Saci_0909 [V49T]. (F) Quantification of the mutant β active subunit Saci_0909 [V49T] mutant proteasome assembly's sensitivity to bortezomib assay, showing Urm1(x3)-GFP degradation when incubated with different concentrations of bortezomib. Error bars represent means ± SD from N = 3.

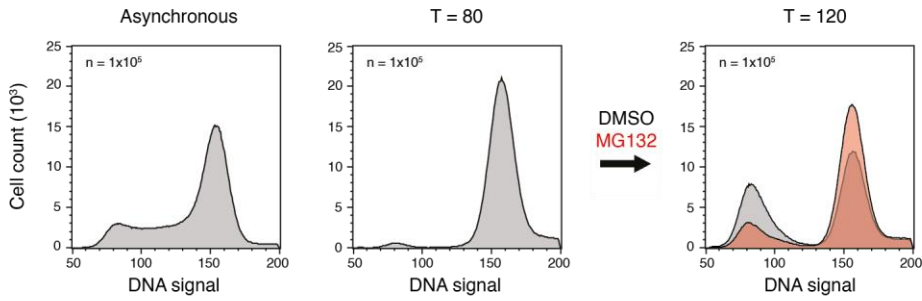
Supplementary Figure 4 Cell cycle responses to proteasomal inhibition



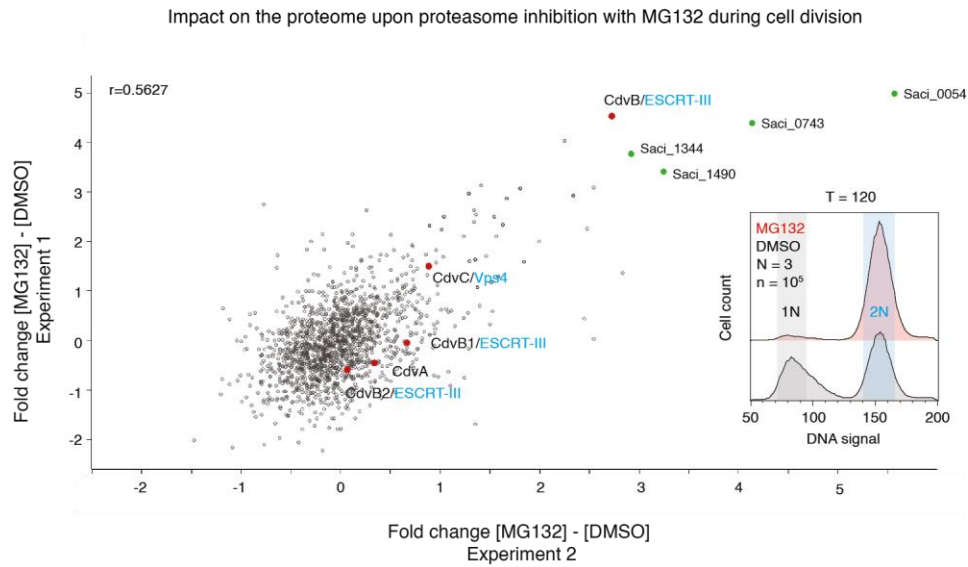
Supplementary Figure 4 Cell cycle responses to proteasomal inhibition. (A) Graph with the distribution of cells with 1N and 2N DNA content in a population following acetic acid synchronisation and release. Error bars represent means \pm SD from N = 3, n = 10^5 . (B) Graph with the distribution of cells with 1N and 2N DNA content in a population following bortezomib treatment of synchronised pre-division cells 80 min after release. Error bars represent means \pm SD from N = 3, n = 10^5 . (C) Flow cytometry histograms showing the number of cells with 1N and 2N DNA content in an STK population after acetic acid synchronisation and bortezomib treatment pre-division. EdU was added to the synchronised population 80 min after release from acetic acid, and bortezomib was added 100 min after release from acetic acid. N = 3, n = 10^6 . Representative histograms shown. (D) Flow cytometry scatterplots showing the individual cells' EdU content vs DNA content from a synchronised STK population 140 minutes after release. The cells had been treated with DMSO or bortezomib, respectively, 100 min after release. The red quadrant shows the S-phase cells with EdU incorporated. Each blue spot represents a single cell, the density gradient going from blue to red. Representative blot shown, N = 3 n = 10^6 . (E) Flow cytometry histograms showing the number of cells with 1N and 2N DNA content in a population following acetic acid synchronisation and bortezomib treatment 120 min after release (post-division). N = 3, n = 10^6 .

Supplementary Figure 5 Proteasomal inhibition with MG132

A



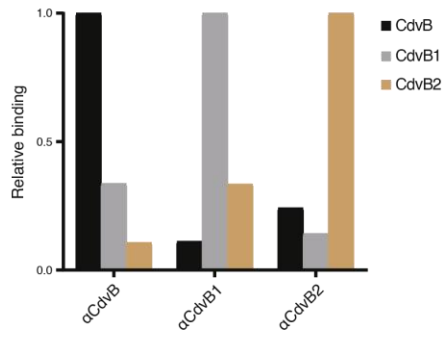
B



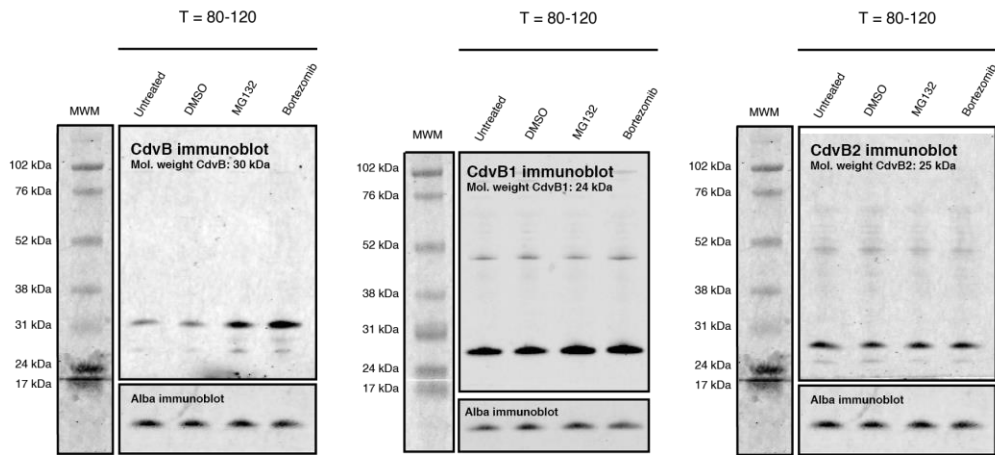
Supplementary Figure 5 Proteasomal inhibition with MG132. (A) Flow cytometry histograms showing the distribution of cells with 1N and 2N DNA content in an asynchronous population (left), a population after release from acetic acid synchronisation but prior to division (middle), and a pre-division synchronised population treated with MG132 or DMSO for 40 min. Representative histograms shown. $N = 3$, $n = 10^5$. (B) Mass spectrometry scatterplot correlating two independent replicates showing the difference in proteomes of pre-division synchronised cells treated with MG132 (1) or DMSO (2) for 40 min. Protein values were measured as the ratio of TMT intensities subtracting \log_2 transformed values of sample (2) from sample (1). The top 5 hits are highlighted in green (except CdvB) and labelled with *S. acidocaldarius* gene extensions. See supplement for complete tables with the data from three independent experiments. The insert shows two representative histograms of the MG132 and DMSO treated samples.

Supplementary Figure 6 *S. acidocaldarius* ESCRT-III homologue antibody specificities

A

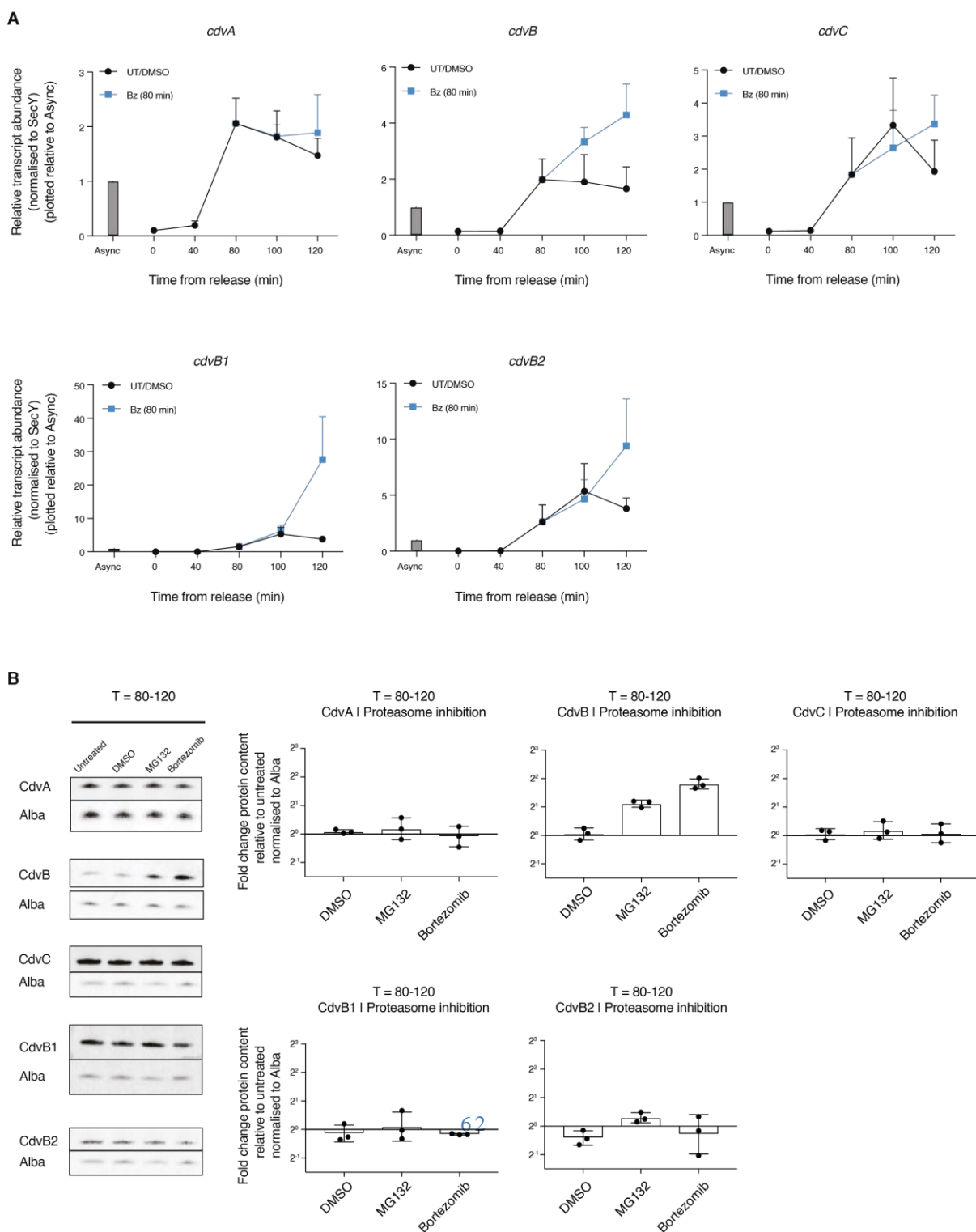


B



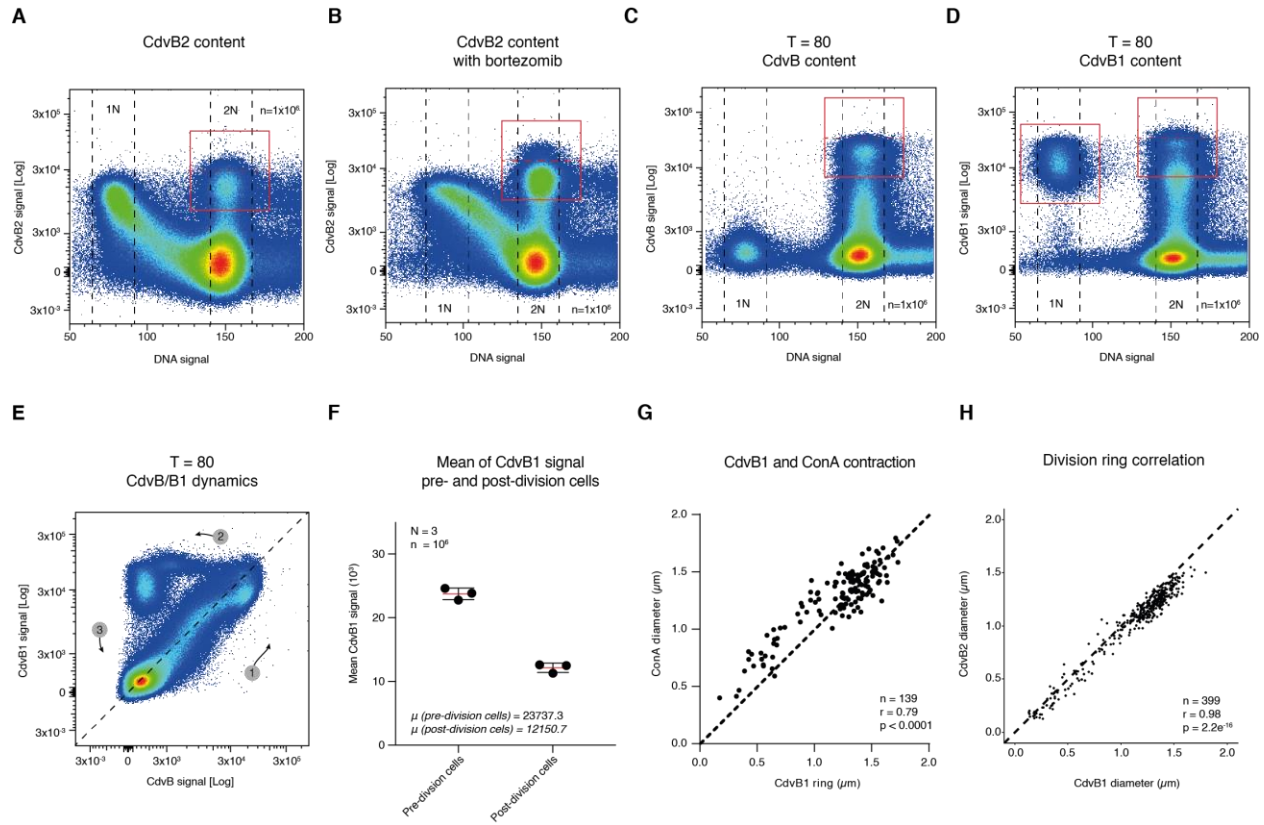
Supplementary Figure 6 S. acidocaldarius ESCRT-III homologue antibody specificities. (A) In vitro ELISA analysis of CdvB, CdvB1 and CdvB2 antibody specificities. CdvB (black), CdvB1 (grey) or CdvB2 (beige) was coated onto a well before detection with antibodies, shown as α Target. (B) Full western blots for synchronised cells in the presence and absence of proteasome inhibitors, probing with CdvB, CdvB1 and CdvB2 antibodies. These immunoblots show that the antibodies for CdvB, CdvB1, and CdvB2 detect proteins at the appropriate molecular weights. Cut-outs of the proteins reported here are shown again quantified in Figure S7B.

Supplementary Figure 7 *cdv* transcript and protein level response to proteasomal inhibition



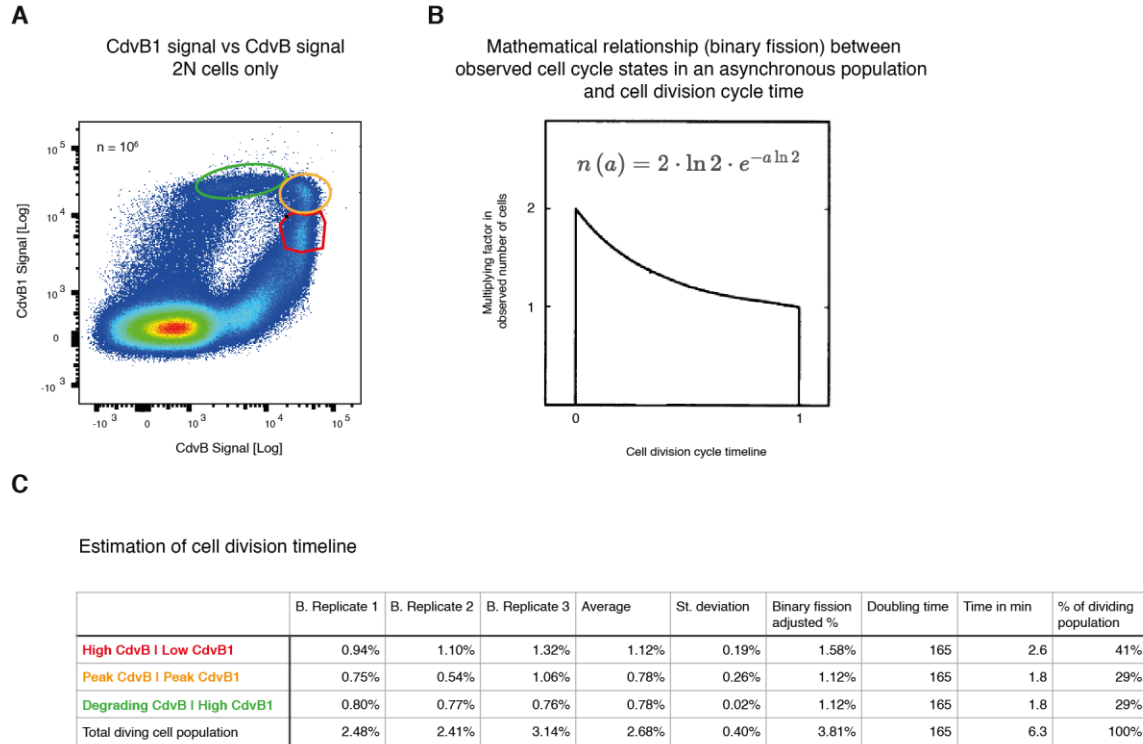
Supplementary Figure 7 Cdv RNA transcript and protein level response to proteasome inhibition. (A) Time course showing qPCR transcript abundance of Cdv proteins in an acetic acid synchronised population treated with bortezomib or DMSO 80 min after release (pre-division). Transcript levels were normalised to *secY* (non- cyclical control gene) and plotted relative to the 'asynchronous' condition. Error bars represent means \pm SD from N = 3. **(B)** Left, western blots of CdvA, CdvB, CdvC, CdvB1, and CdvB2 protein levels, with Alba as a loading control. All samples were taken 120 min after release from acetic acid synchronisation, after having been left untreated or treated with DMSO, MG132, or bortezomib for 40 minutes (i.e. from T80-120). Representative blots shown. Right, quantification of the western blots shown as fold change of protein relative to the untreated condition and normalised with Alba. Error bars represent means \pm SD from N = 3.

Supplementary Figure 8 Targeted degradation of CdvB triggers constriction via CdvB1 and CdvB2



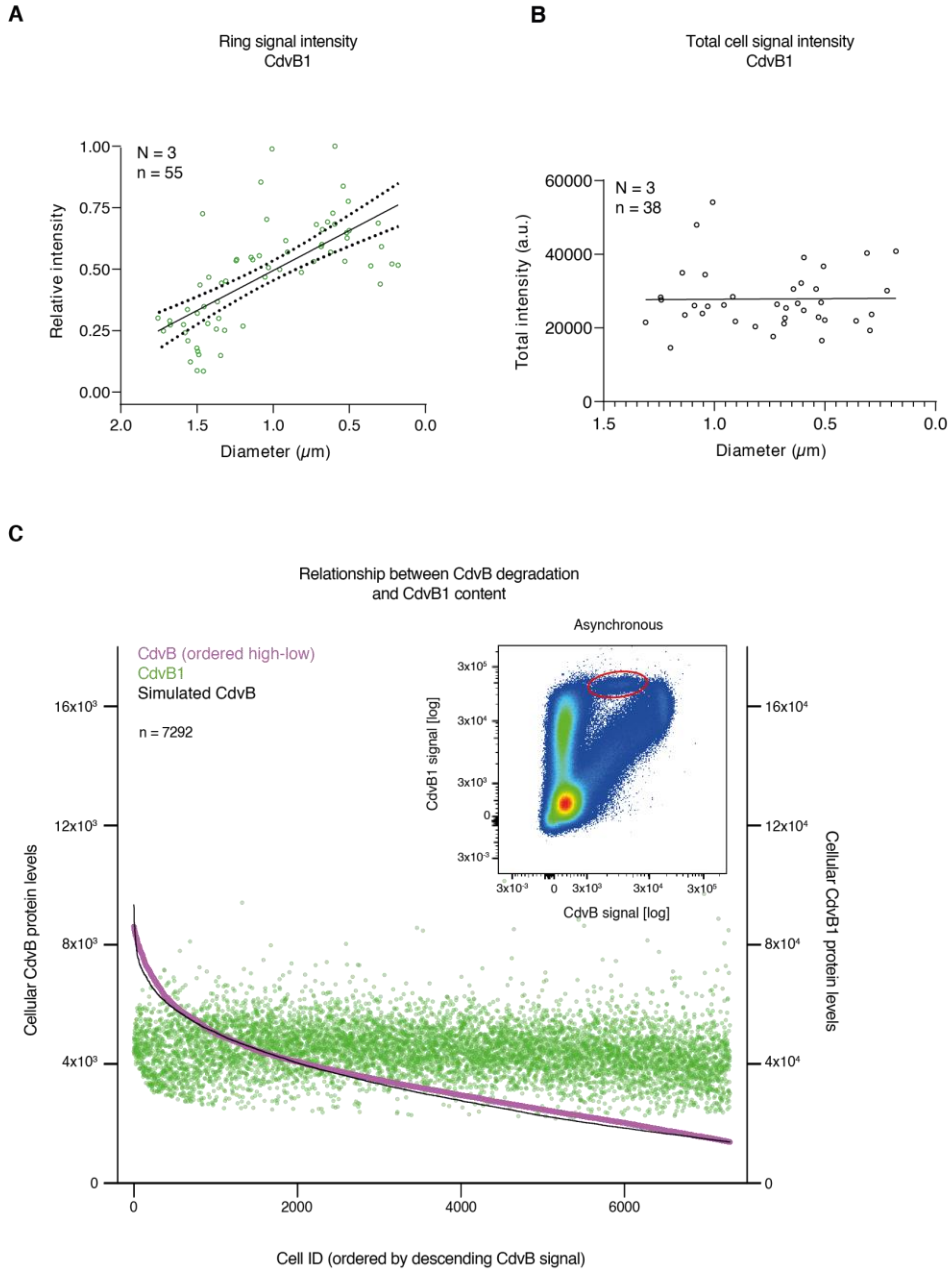
Supplementary Figure 8 Targeted degradation of CdvB triggers constriction via CdvB1. **(A)** Flow cytometry scatterplot with CdvB2 signal versus DNA signal for an asynchronous population. Red insert frames the “mitotic” cells with high signal. Each blue spot represents a single cell, the density gradient going from blue to red. Representative plot shown. N = 3, n = 10⁶. **(B)** Flow cytometry scatterplot with CdvB2 versus DNA signal for an asynchronous culture treated with bortezomib. Red insert frames “mitotic” cells with high signal. Each blue spot represents a single cell, the density gradient going from blue to red. Representative plot shown. N = 3, n = 10⁶. **(C and D)** Flow cytometry scatterplots with CdvB and CdvB1 signal, respectively, against DNA signal for a synchronous culture 80 min after release, in which fewer than 5% of cells have divided. The red inserts frame “pre-division” cells with high signal and in **(D)** a second red square frames the recently divided cells with 1N DNA signal and high levels of CdvB1. Each blue spot represents a single cell, the density gradient going from blue to red. Representative plots shown. N = 3, n = 10⁶. **(E)** Flow cytometry scatterplot of CdvB1 vs CdvB signal for a synchronous culture 80 min after release in which fewer than 5% of cells have divided. Note the accumulation and loss of CdvB and CdvB1 protein indicated with the numbers/arrows. Each blue spot represents a single cell, the density gradient going from blue to red. Representative plots shown. N = 3, n = 10⁶. **(F)** Quantification of CdvB1 signal in pre-division cells. Error bars represent means ± SD from N = 3, n = 10⁶. **(G)** Correlative analysis of S-layer diameter as identified by concanavalin A vs CdvB1 ring diameter from widefield microscopy. N = 3, n = 139. **(H)** Correlative analysis of CdvB2 and CdvB1 ring diameters from SRRF super resolution microscopy. All quantifications cover more than 6 fields of view and 3 biological replicates. N = 3, n = 399.

Supplementary Figure 9 Estimation of the timeline of cell division in *S. acidocaldarius*



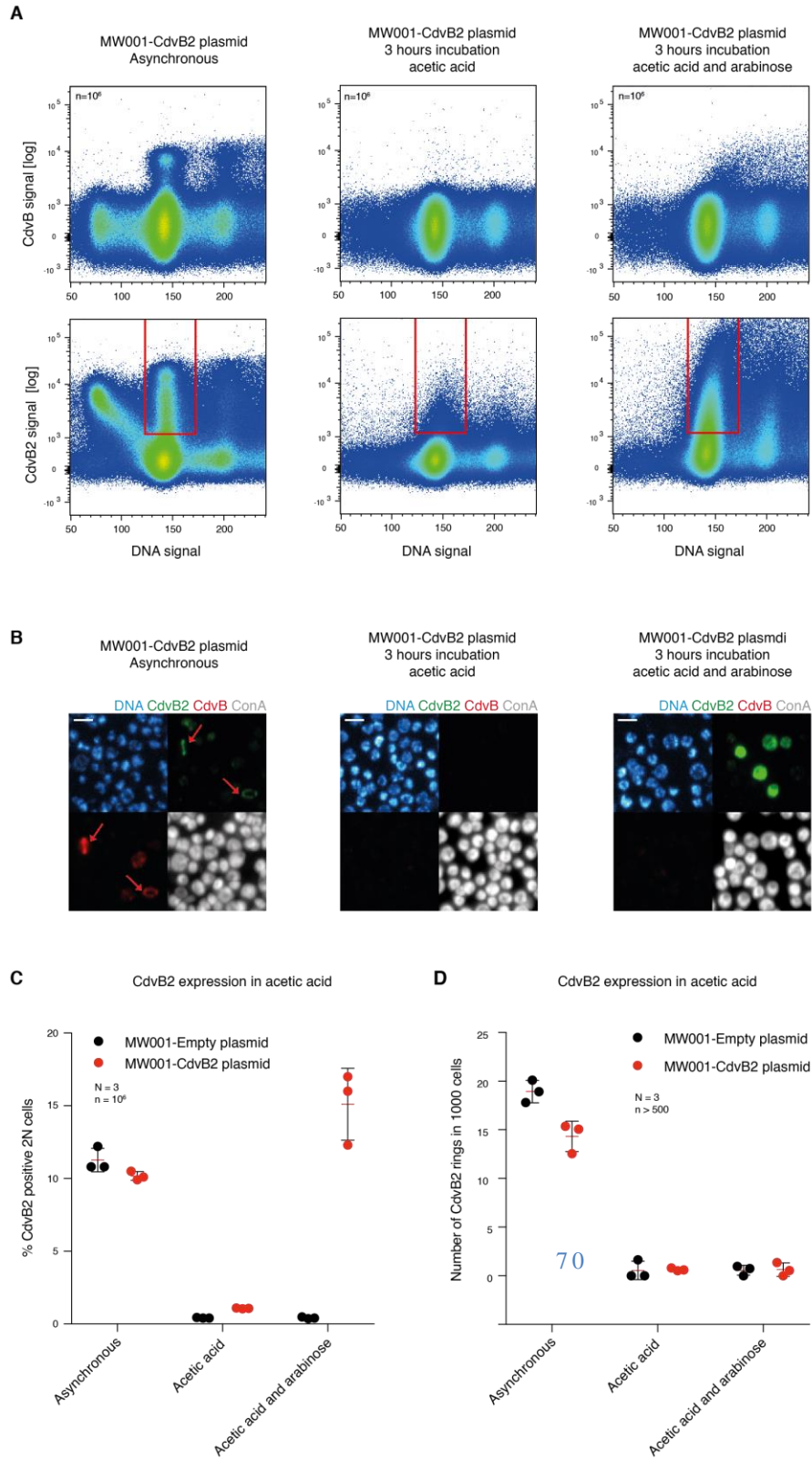
Supplementary Figure 9 Estimation of the timeline of cell division in *S. acidocaldarius*. **A)** Flow cytometry scatterplot of CdvB1 vs CdvB signal for an asynchronous population in which all cells with less than 2N DNA signal have been removed. Red insert: population of cells with peak CdvB and low CdvB1 signal (corresponding to cells with CdvB+ and CdvB1- rings). Yellow insert: population of cells with peak CdvB and peak CdvB1 signal (corresponding to cells with CdvB+ and CdvB1+ rings). Green insert: population of cells degrading CdvB and with peak CdvB1 signal (corresponding to cells with CdvB- and CdvB1+ rings). Each blue spot represents a single cell, the density gradient going from blue to red. Representative plot shown. $N = 3$, $n = 10^6$. **B)** Graphical representation of the mathematical relationship between observed cell cycle states in an asynchronous population growing exponentially with binary fission and the actual cell cycle time. Note that the earliest stage of the cell cycle will be two times more frequently observed than the latest state of the cell cycle. The defined integral of function $n(a)$ returns the observed percentage of cells with respect to the percentage covered by the cell cycle timeline (0 being the start and 1 the end of the cycle). **C)** Estimation of the cell division timeline on the basis of the CdvB and CdvB1 dynamics. Note the stability of the percentage of cells degrading CdvB and the variation in the percentage of cells with CdvB-CdvB1 rings and CdvB rings alone. Overall the process of division appears to take about 6.3 minutes and the actual cell constriction (coinciding with CdvB degradation) about 1.8 minutes. The number of cells with peak CdvB content observed by flow cytometry corresponds to the percentage of cells with rings as observed by microscopy. $N = 3$, $n = 10^6$.

Supplementary Figure 10 Degradation and disassembly dynamics of the ESCRT-III cell division ring



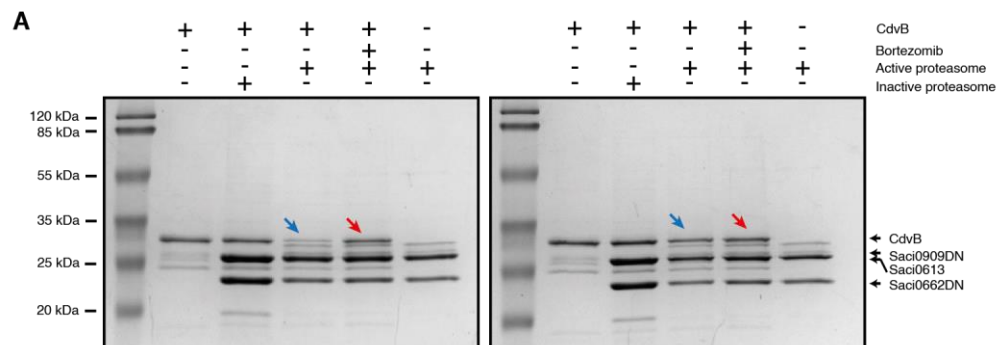
Supplementary Figure 10 ESCRT-III dynamics during cell division. **A)** Graph plotting the CdvB1 ring signal intensity as a function of its diameter. $N = 3$, $n = 55$. **B)** Graph plotting the total CdvB1 signal of a cell as a function of its diameter. $N = 3$, $n = 38$. The images studied for these datasets were obtained with iSIM (unprocessed) widefield microscopy **C)** Graph comparing CdvB protein level (purple) and CdvB1 protein level (green) present in cells that are degrading CdvB and about to divide. The CdvB curve follows a power law with exponent $\alpha=0.22$ reproduced with stochastic sampling in black which supports the understanding that CdvB is rapidly degraded to trigger cell division (see methods). The inset shows the CdvB1 vs CdvB signal in an asynchronous population of cells. The population of cells degrading CdvB highlighted in red is the same one plotted in the graph. Each blue spot represents a single cell, the density gradient going from blue to red, $n = 10^6$.

Supplementary Figure 11 CdvB2 alone does not assemble into a division ring



Supplementary Figure 11 CdvB2 alone does not assemble into a division ring. (A) Top, flow cytometry scatterplots with CdvB signal vs DNA signal for MW001 cells with an arabinose-inducible CdvB2 overexpression plasmid. Bottom, same as top, but for CdvB1 vs DNA signal. Left, the untreated asynchronous population. Middle, the population after three hours of acetic acid treatment. Right, the population after three hours of acetic acid and arabinose treatment. The red insert shows the CdvB2 positive cells in a 2N state. Each blue spot represents a single cell, the density gradient going from blue to red. Representative scatterplots shown, $n = 10^6$. (B) unprocessed iSIM widefield microscopy images the cells under the three conditions stained for DNA, CdvB2, CdvB and ConA. The red arrows indicate division rings in the untreated asynchronous population. (C) Quantification of the percentage of 2N cells with high levels of CdvB2 in the three conditions. Error bars represent means \pm SD from $N = 3$, $n = 10^6$. (D) Quantification of the number of CdvB2 rings in 1000 in the three conditions. Error bars represent means \pm SD from $N = 3$, $n = 10^6$.

Supplementary Figure 12 Degradation of CdvB *in vitro*



Supplementary Figure 12 In vitro degradation assay of CdvB by the 20S *S. acidocaldarius* proteasome in conditions with and without bortezomib. (Lane 1) CdvB only control. (Lane 2) Using the inactive 20S proteasome (Saci_0613/Saci_0662ΔN) on the CdvB substrate. (Lane 3) Using the active 20S proteasome (Saci_0613/Saci_0662ΔN/Saci_0909ΔN) on the CdvB substrate in the absence of the bortezomib inhibitor. (Lane 4) As in Lane 3 but in the presence of 50 μM Bortezomib. (Lane 5) The active 20S proteasome alone as a no substrate control. Assays contained 30 μg of the 20S proteasomal complex incubated with 4 μg CdvB substrate for 120 minutes at 63°C. Two biological replicates shown. Blue arrows mark CdvB levels with the active proteasome in the absence of bortezomib. Conversely, red arrows mark the CdvB levels with the active proteasome in the presence of 50 uM bortezomib.

Supplementary Figure 13 PAN-WalkerB-overexpression constructs. (A) The synthetic gene construct of PAN-WalkerB (uppercase) with the 5' PciI and 3' XhoI cut sites highlighted in red. The Walker B motif and mutation [E237Q] is highlighted in yellow. (B) Plasmid map of pSVA-araFX-PAN-WkB-HA, with genes highlighted.

Supplementary Figure 14 CdvB2-overexpression constructs. (A) The synthetic gene construct of CdvB2 (uppercase) with the 5' NcoI and 3' XhoI cut sites highlighted in red. (B) Plasmid map of pSVA-araFX-CdvB2, with genes highlighted.

Supplementary Movie 1 Constriction simulation without filament disassembly

<File added separately>

Supplementary Movie 2 Constriction simulation with filament disassembly

<File added separately>

Supplementary Table 1 Data collection and refinement statistics for the Saci_0613/Saci_0662ΔN Proteasome

Data Collection

Space group P 21 21 21

Cell Dimensions

a, b, c (Å) 108.289 193.654 323.671
a, b, g (°) 90 90 90
Wavelength (Å) 0.9801
Resolution range (Å) 48.19 - 3.698 (3.83 - 3.698) *
Mean I/sigma 5.64 (1.56)
Completeness (%) 99.21 (96.06)
Wilson B-factor 82.08
Multiplicity 2.0 (2.0)

Refinement

Total reflections 144662 (13665)
Unique reflections 73138 (6972)
R-work 0.2873 (0.3422)
R-free 0.3343 (0.3992)
Reflections used in refinement 73060 (6967)
Reflections used for R-free 3676 (347)
Number of non-hydrogen atoms 41436
Macromolecules 41436
Protein residues 5391
RMS (bonds) 0.002
RMS (angles) 0.57
Ramachandran favoured (%) 94.7
Ramachandran allowed (%) 4.96
Ramachandran outliers (%) 0.34
Rotamer outliers (%) 0.61
Clashscore 11.63
Average B-factor 76.94

*Statistics for the highest-resolution shell are shown in parenthesis

Supplementary Table 2 Mass spectrometry tables with Cdv proteins

(A)

	CdvA	CdvB	CdvC	CdvB1	CdvB2
Experiment 1					
Log2 [bortezomib] - Log2 [bortezomib wash-out]	0.36	2.53	-0.07	-0.44	0.32
Experiment 2					
Log2 [bortezomib] - Log2 [bortezomib wash-out]	0.26	2.84	0.54	1.03	0.53
Experiment 3					
Log2 [bortezomib] - Log2 [bortezomib wash-out]	-0.40	2.44	-0.08	-0.14	0.11

(B)

	CdvA	CdvB	CdvC	CdvB1	CdvB2
Experiment 1					
Log2 [MG132] - Log2 [DMSO]	-0.30	1.44	-1.08	-0.26	-0.25
Experiment 2					
Log2 [MG132] - Log2 [DMSO]	-0.45	4.53	1.51	-0.04	-0.58
Experiment 3					
Log2 [MG132] - Log2 [DMSO]	0.34	2.72	0.89	0.67	0.07

Supplementary Table 3 List of antibody host species and secondary antibodies

Target	Primary antibody host	Secondary antibody
CdvB	Rabbit	Goat anti-Rabbit AlexaFluor 546 (Invitrogen, A11035)
CdvB1	Chicken	Goat anti-Chicken AlexaFluor 488 (Invitrogen, A11039)
CdvB1	Chicken	Goat anti-Chicken AlexaFluor 555 (Invitrogen, A21437)
CdvB2	Guinea Pig	Goat anti-Rabbit AlexaFluor 546 (Invitrogen, A11073)

Supplementary Table 5 List of primers used for RT-qPCR analysis

<i>Saci</i> annotation	Gene	Sequence
Forward Saci_0574	<i>secY</i>	ACTCTTGCTTGACGAGATGATAC
Reverse Saci_0574	<i>secY</i>	ACTCTGTACGGAGACTATTCCA
Forward Saci_1374	<i>cdvA</i>	GGACAGATGGAGAAGATAAGGAAG
Reverse Saci_1374	<i>cdvA</i>	TGAGCAACTTGGTCCTCTATTG
Forward Saci_1373	<i>cdvB</i>	ACTGGTGCATTAAGCGAGAA
Reverse Saci_1373	<i>cdvB</i>	TTGGTAACTCTGAAGGTGGATG
Forward Saci_1372	<i>cdvC</i>	GCTGTAGCTAATGAGATCGACTCATATT
Reverse Saci_1372	<i>cdvC</i>	CAGCCTCGCCTAGCCACTTA
Forward Saci_0451	<i>cdvB1</i>	GGTGAAGTGAAGGTTTACA
Reverse Saci_0451	<i>cdvB1</i>	CTGTCTTGCCTCTGGTGAATAG
Forward Saci_1416	<i>cdvB2</i>	CTCTTCTCCAGAGGCAAGAAAAG
Reverse Saci_1416	<i>cdvB2</i>	CCGAAGTTGCAAATGATGGTAAA